Geochimica et Cosmochimica Acta xxx (xxxx) xxx

Contents lists available at ScienceDirect

Geochimica et Cosmochimica Acta

journal homepage: www.elsevier.com/locate/gca

Symplectite formation in ultramafic achondrites by impact percolation of a sulfide melt

Z. Váci [a,*], P.M. Kruttasch [b], M.J. Krawczynski [a], R.C. Ogliore [c], K. Mezger [b]

[a] Department of Earth and Planetary Sciences, Washington University in St. Louis, MO, USA
[b] Institut für Geologie, Universität Bern, Switzerland
[c] Department of Physics, Washington University in St. Louis, MO, USA

ARTICLE INFO

Associate editor: Thorsten Kleine and Liping Qin

Keywords:
Symplectite
Impact
Dunite
Achondrite
Lherzolite
Chromite
Veins
Experimental petrology
Sulfide
Cr Isotopes

ABSTRACT

The ungrouped dunitic achondrite Northwest Africa (NWA) 12217 contains symplectic spinel-pyroxene veins that are mineralogically identical to symplectites in other ultramafic planetary materials. The morphology and amount of chromite present in these features relative to the Cr in their olivine hosts suggest an exogenous origin. Petrological experiments show that a Cr laden sulfide liquid reacts with olivine to produce pyroxene by scavenging Mg and Fe from olivine to crystallize chromite. The liquid infiltrates cracks and grain boundaries within the olivine and produces a vein-like symplectic chromite-pyroxene mineralogy similar to that observed in NWA 12217. This process is likely responsible for forming the symplectites in the related ultramafic achondrites NWA 12319, 12562, and 13954, along with many other achondrites. The nucleosynthetic Cr isotopic composition of chromites appears to be in disequilibrium with that of silicates in NWA 12217, suggesting that the liquids responsible for the symplectite forming reaction are at least partially sourced from a different parent body and result from an impact.

1. Introduction

Spinel-pyroxene symplectites are fine-grained vermicular intergrowths of various spinel compositions and high- and low-Ca pyroxenes. These features are prevalent in terrestrial and extraterrestrial mafic to ultramafic rocks, but their formation conditions have remained quite enigmatic (e.g. Bell et al., 1975). Despite their uniform morphology across diverse petrologic contexts, there does not appear to be a unique mechanism that can generate these features. Petrogenetic interpretations have ranged from primary igneous crystallization to subsolidus interactions with late-stage melts and cooling effects, along with changes in temperatures and pressures that result in metamorphic reactions between various phases.

Spinel-pyroxene symplectites occur in two different morphologies that can be attributed to separate processes, and these are defined as Type I and Type II by Khisina and Lorenz (2015). This study refers to oriented, μm-scale, lamellar or needle-like spinel-pyroxene symplectites embedded in olivine as Type I, and the usually larger irregularly shaped spinel-pyroxene symplectites in olivine as Type II. Both Type I and Type II symplectites have been identified in olivine-bearing lunar rocks (Gooley et al., 1974; Bell et al., 1975; Dymek et al., 1975; Elardo et al., 2012) and ungrouped achondrites (Goodrich and Righter, 2000). Type II symplectites are also found within olivine grains and along grain boundaries both in harzburgitic clasts in howardites (Lunning et al., 2015; Hahn et al., 2018), and in ungrouped dunitic to lherzolitic meteorites associated with the HED (howardite-eucrite-diogenite) parent body (Vaci et al., 2021).

This study examines the Type II spinel-pyroxene symplectites identified in the ungrouped ultramafic achondrites NWA 12217, 12319, 12562, and 13954 (Vaci et al., 2021), which for simplicity will be referred to as symplectites. Sample analysis focuses on the monomict dunite breccia NWA 12217, as it also contains "symplectic" veins that are compositionally identical to the symplectites. As such, the morphology, mineralogy, and petrology of the veins provide insight into the formation mechanisms of the symplectites. Two sets of experiments were performed at pressures of one atmosphere and 1 GPa in order to examine the petrogenesis and replicate the mineralogy of the symplectites and veins.

* Corresponding author.
E-mail address: vaci@wustl.edu (Z. Váci).

https://doi.org/10.1016/j.gca.2024.08.011
Received 20 February 2024; Accepted 10 August 2024
Available online 13 August 2024

Chromium isotopes were determined in whole-rock (WR) and separated chromite and silicate fractions of NWA 12217 to constrain (1) their ε^{54}Cr compositions and (2) the time of chemical fractionation using the short-lived ^{53}Mn-^{53}Cr decay system. The heterogeneous distribution of the most neutron-rich Cr isotope (^{54}Cr) among meteorites and their constituents has long been recognized and used as tool to define early Solar System reservoirs and to understand mixing of material derived from these reservoirs. Due to the homogeneous distribution of ^{53}Mn and ^{53}Cr in the early Solar System, the short-lived ^{53}Mn-^{53}Cr decay system with a half-life of 3.7 ± 0.4 Ma (Honda and Imamura, 1971) is of particular interest to quantify the temporal evolution of Solar System material in the first ~ 20 Ma of its history. Ultramafic achondrites, such as NWA 12217, are suitable targets for the application of the ^{53}Mn-^{53}Cr system due to their relatively high abundance of Cr and variable Mn/Cr in different mineral phases.

The first aim of this study is to characterize naturally occurring symplectites in extraterrestrial samples so that the field of potential formation mechanisms can be narrowed. The second aim is to present a set of experiments demonstrating a novel formation mechanism that applies specifically to the symplectites in the ungrouped ultramafic achondrites. This mechanism is then used to reevaluate symplectite formation mechanisms in the many different petrological contexts that symplectites occur in.

2. Background

Although the present study focuses on a very specific subset of symplectites, the conclusions drawn have broad applications to a wide variety of natural environments. Therefore, a summary of previous research on symplectite formation is warranted.

2.1. Symplectites in terrestrial rocks

On Earth, symplectites are found in mantle xenoliths, layered intrusions, kimberlites, and metamorphic rocks, and are thought to form either by crystallization from a late-stage melt, interaction of a melt or fluid with a mineral, mineral–mineral reactions, or breakdown of a preexisting phase due to changes in P-T conditions. In mantle peridotites, spinel-pyroxene symplectites can form as breakdown products of garnets formed at originally greater depths (Dawson and Smith, 1975; Godard and Martin, 2000; Morishita and Arai, 2003). These can contain additional phases such as phlogopite or amphibole, leading to the suggestion that they are indicators of metasomatism by a hydrous fluid (Field, 2008).

Symplectites are also commonly found in the norites, troctolites, and gabbros in layered igneous intrusions. Here they form from the oxidation of olivine, producing an oxide phase (most commonly magnetite or ilmenite) and one or more mafic silicates such as pyroxene, amphibole, or biotite (Holness et al., 2011; Efimov and Malitch, 2012; Keevil et al., 2020). Although there is no consensus on how they form, possible mechanisms include exsolution of incompatible species during cooling (Moseley, 1984), sub-solidus olivine oxidation (Efimov and Malitch, 2012), and dehydration of hydrous olivine that results in oxidation (Khisina and Lorenz, 2015). Alternative hypotheses to these autochthonous mechanisms include super-solidus reactions with late-stage liquids during the final stages of crystallization (Holness et al., 2011; Keevil et al., 2020) and fluid-mediated metasomatic replacement reactions (Putnis and Austrheim, 2010; Spruzeniece et al., 2017). A common feature of symplectites surrounding mineral phases is that the symplectite forming reaction is not isochemical, but instead it requires the addition or removal of components (e.g. Spruzeniece et al., 2017).

2.2. Symplectites in extraterrestrial rocks

The discovery of chromite-pyroxene symplectites in lunar rocks has generated significant debate among planetary scientists since the Apollo missions (e.g. Bell et al., 1975). Chromite-bearing symplectites appear enclosed in olivine phenocrysts in mare basalts and lunar dunites, along grain boundaries in lunar troctolites, and as lamellar or needle-like inclusions within olivine phenocrysts in various lunar rocks. One potential formation mechanism for symplectites along grain boundaries is via a reaction between olivine and plagioclase, with excess Cr diffusing out of olivine to form chromite (Gooley et al., 1974; Bell et al., 1975). However, the olivines in lunar troctolite 76535, in which such features are abundant, are too depleted in Cr to form such Cr-rich features, and instead are hypothesized to require an exogenous source of Cr such as a metasomatic fluid (Elardo et al., 2012).

Other explanations for lunar symplectites include the crystallization of late-stage melts, the breakdown of individual mineral phases such as garnet, and solid-state diffusion and precipitation out of host olivine (Bell et al., 1975). Chromite-pyroxene symplectites generally contain too much Cr to have crystallized from any realistic silicate melt composition (Elardo et al., 2012; Hahn et al., 2018), although it is hypothesized that slowly cooled late stage melts could form these textures in the presence of primary chromite grains (Dymek et al., 1975). Likewise, the garnet breakdown reaction is hypothetical, as unlike terrestrial samples, spinels with symplectic coronae are absent from lunar rocks. While this could result from the complete transformation of garnet, this mineral has never been identified in a lunar rock and can only exist deep within the lunar mantle.

Expulsion of minor elements such as Cr and Al out of the olivine lattice is a viable mechanism for the formation of lamellar or needle-like symplectites that form along crystallographic axes and produce depletion "halos" of these elements in their host olivine (Gooley et al., 1974; Bell et al., 1975; Khisina et al., 2011). Such lamellar features are also observed in olivines in nakhlites and chassignites (Mikouchi et al., 2000). On Earth and Mars, this mechanism usually involves the oxidation of Fe in olivine to form magnetite; lunar symplectites instead develop through oxidation of divalent Cr in olivine to form chromite.

Both Type I and II symplectites have also been identified in ungrouped achondrites and howardites. The ungrouped achondrite Queen Alexandria Range (QUE) 93148 contains Type I and II symplectites, although the vast majority are Type II with additional phases such as sulfides, phosphates, and FeNi metal (Goodrich and Righter, 2000). While the formation of the Type I symplectites was attributed to exsolution of Cr and Ca from olivine, Type II symplectites were suggested to have formed from trapped silicate and metallic melts that oxidized as they cooled (Goodrich and Righter, 2000). Chromite-pyroxene symplectites are also found within ultramafic HED samples and mesosiderites, which although not likely to be sourced from Vesta, show associations with HED material (Greenwood et al., 2015; Iannini Lelarge et al., 2022). These include Type I symplectites within the mesosiderite Budulun and Type II symplectites within the howardite Dhofar 018, where they were hypothesized to have formed by dehydrogenation of previously hydrated olivine that resulted in oxidation (Khisina and Lorenz, 2015). This mechanism is difficult to reconcile with conditions inside a parent body as depleted in volatiles as the HED parent body (e.g. Mittlefehldt, 2015).

The ureilites are another group of extraterrestrial samples in which spinel-pyroxene symplectites have been identified. Olivines in LaPaz Icefield (LAP) 03587 and Cumulus Hills (CMS) 04048 host ≤μm-sized oriented Type I symplectites whose formation was attributed to exsolution of Cr^{3+} from olivine due to contraction upon cooling (Goodrich

et al., 2013). The pyroxene formed by this exsolution reaction preferentially incorporated trace elements incompatible in olivine, such as Ca, similarly to magnetite-pyroxene Type I symplectites in terrestrial olivine (Moseley, 1984). In Lewis Cliff (LEW) 88774, NWA 766, and NWA 3109, symplectic bands composed of chromite, high-Ca pyroxene, and glass were found surrounding primary phases such as olivine and orthopyroxene (Goodrich et al., 2014). The formation of such features was attributed to rapid heating, decompression, reduction, and partial melting by impact, which moved Cr from primary chromites into a Si-rich melt by reduction of FeO. This melt then reacted with primary silicates along grain boundaries to produce the symplectic bands (Goodrich et al., 2014).

Finally, the symplectites most similar and relevant to those discussed in the present study were identified in harzburgitic clasts in howardites (Lunning et al., 2015; Hahn et al., 2018). The formation of these features was attributed to crystallization of a trapped melt that had to contain a metallic component in addition to any silicate melt (Hahn et al., 2018), since silicate melts cannot accommodate enough Cr at the oxygen fugacity estimated for the differentiation of the HED parent body (Elardo et al., 2012). Dominion Range (DOM) 10839 contains evidence of the silicate melt component in the form of an apparentlly Cr-rich "melt" found adjacent to symplectites, as well as FeNi grains that contain Cr (Hahn et al., 2018). Microprobe analyses of the "melt" phase show between 1 and 12 wt% Cr_2O_3, but this unrealistically high amount of Cr in a silicate melt is probably attributable to either beam overlap with adjacent chromite or fluorescence of Cr in adjacent chromite by X-rays emitted by Fe excitation in the melt.

3. Methods

3.1. Electron microscopy

All electron microbeam analyses were performed at Washington University in St. Louis. Electron probe microanalysis (EPMA) of natural and experimental samples was performed using a JEOL JXA-8200 electron microprobe equipped with five wavelength-dispersive spectrometers. Analyses were acquired with the software Probe for EPMA (Donovan et al., 2012) that applies a mean atomic number (MAN) background correction obtained from a large standard suite. Analytical conditions for sample acquisition were 15 kV accelerating voltage, 25 nA beam current, and a spot diameter of 1 μm for mineral analyses and 20 μm for bulk symplectite analyses. The instrument was standardized for the analysis of Si, Ti, Al, Cr, Fe, Mn, Ni, Mg, Ca, Na, K, and S using Amelia albite, synthetic forsterite, Alaska anorthite, Gates wollastonite, Durango apatite, Madagascar orthoclase, synthetic TiO_2, synthetic Cr_2O_3, synthetic tephroite, Elba hematite, synthetic Ni-olivine, and Taylor pyrite. Standardization accuracy was periodically verified by analysis of a secondary standard, Kakanui hornblende.

Scanning electron microscopy (SEM) was conducted using a Tescan Mira3 with a Schottky-type field-emission gun (FEG) and an EDAX Octane Plus (30 mm^2 silicon-drift detector) energy-dispersive X-ray system. Accelerating voltages of 10–20 kV and beam currents of 1–3 nA were used for backscattered electron (BSE) imaging and X-ray mapping. X-ray maps were collected and processed using EDAX TEAM software. A thin section of NWA 12217 was chemo-mechanically polished using colloidal silica for electron backscatter diffraction (EBSD). The crystallographic orientations of olivine grains in NWA 12217 were determined by EBSD analysis using a Thermofisher Quattro S environmental SEM equipped with an Oxford Symmetry EBSD detector. Operating conditions were low vacuum, a working distance of 19–20 mm, an accelerating voltage of 20 kV, and a step size of 5 μm.

A single 10 × 20 μm section was extracted from NWA 12217 and milled to ~ 100 nm thickness using a Ga^+ focused ion beam (FIB) mode on an FEI Quanta 3D Dual Beam electron microscope. A 30 kV accelerating voltage and beam currents of 0.1–3 nA were used for milling and thinning of the sample. The section was cleaned of amorphous material using a final thinning step performed at 5 kV and 53 pA. The sample was imaged using a JEOL JEM-2100F FEG scanning transmission electron microscope (STEM), operating in STEM mode with an accelerating voltage of 200 kV and a 0.5 nm spot size.

3.2. Micro-XCT

Micro-XCT analyses were performed at the Washington University Center for Cellular Imaging. Samples were imaged on a Zeiss Versa 520 X-ray microscope at 140 keV accelerating voltage and 10 W, using either a 0.4x flat-panel detector or a 4x scintillated objective. The field of view was enhanced via Wide Stitch or Vertical Stitching, as needed. 1600 projections were reconstructed, and resultant tomograms were filtered via a non-local means filter to reduce noise. Final volumes were visualized in ORS Dragonfly 2022 (Montreal, Québec).

3.3. Petrological experiments

Experimental starting materials for one atmosphere experiments were mixed using reagent-grade synthetic $CaTiO_3$, Fe_2O_3, $Mg(OH)_2$, $CaSiO_3$, and FeS powders in an agate mortar under ethanol. These were pressed into pellets, suspended from rhenium wire loops, and hung from platinum wire inside a Deltech gas mixing furnace. The fO_2 was set to IW-1 by mixing H_2 and CO_2 gases and monitored using a YSZ oxygen sensor. Experiments were quenched by applying a current to the platinum wire which caused it to break and release the experimental charge into deionized water.

Experimental starting materials for 1 GPa experiments were San Carlos olivine and reagent-grade synthetic FeS and Cr^0 powders. The olivine was previously tumbled and visually inspected using a binocular microscope to ensure that it was free of any impurities such as other mineral phases or melt inclusions before being ground and sieved into a 150–250 μm powder. The FeS and chromium powders were mixed in an agate mortar under ethanol. Both reactants were loaded into graphite capsules and pressurized to 1 GPa inside of a 12.5 mm outer diameter piston-cylinder apparatus using a thin lead foil for lubrication, $BaCO_3$ as a pressure medium, and a graphite furnace. Experiments were heated to 900° C and left overnight in order to remove voids and sinter the synthetic powders before they were reacted with the olivine. Temperatures were monitored using a Type C thermocouple and maintained to within 5° C of their target temperatures using a Eurotherm PID controller. Experiments were quenched by cutting the power to the graphite furnace, which cooled the experiment to room temperature at a rate of 120° C/s (Gavrilenko et al., 2019).

3.4. Method for Cr isotope analyses

The whole rock (WR) powder of sample NWA 12217 was divided into two fractions (~50 mg each) for WR analysis and separation of chromites from silicates, sulfides, and metals. For sequential digestion, the first fraction was digested in a first step with concentrated HNO_3 + HF followed by a second step with HNO_3 + HCl on a hotplate at 120 °C for two days each. The acid mixtures, containing silicates, sulfides, and metals, were always separated from the residue after centrifuging for 3 minutes at 3000 rpm. The residue was washed in MilliQ water, centrifuged, and the solution was transferred to the previously separated acids. The combined mixture from Step 1 and 2 was dried down on a hotplate at 90° C and labeled "L1". The residue (labeled "L2"), consisting primarily of chromites, was digested together with the second fraction for WR analyses in a mixture of concentrated HNO_3 + HF in a Parr® bomb at 190 °C for three days to completely digest residual chromite grains. The digests were dried down on a hotplate at 90 °C. All fractions (WR, L1, L2) were then dissolved in 6 mL 0.5 M HNO_3. From each stock solution, 50 μL aliquots were separated and diluted to produce a 1–10 ppb Cr solution for Cr, Mn and Fe elemental analyses. These analyses were performed at the Institute of Geography, University of Bern using a

7700x Agilent ICP-MS. The reported uncertainties for $^{55}Mn/^{52}Cr$ and Fe/Cr are < 5 % for all fractions.

Chromium was purified by three-step cation–anion exchange chromatography, as described in Anand et al. (2022), using 1 to 6 mL of the stock solutions to load ~ 15 µg Cr onto each column. After purification, Cr fractions were redissolved in a mixture of concentrated H_2O_2 + HNO_3 + HCl and dried on a hotplate at 60 to 90 °C to remove organic compounds. Subsequently, the samples were dissolved in concentrated HCl for conversion into chlorides and again evaporated on a hotplate at 90 °C. The purified Cr was finally dissolved in 8 µL 6 M HCl. One µL Cr solution was loaded onto multiple previously degassed Re-filaments with 1.4 µL Al-doped silica gel and 0.8 µL H_3BO_3 (5000 ppm).

Chromium isotopes were measured on a TRITON Plus Thermal Ionization Mass Spectrometer (TIMS) at the Institute of Geological Sciences, University of Bern. Prior to the start of each measurement, the mass of ^{53}Cr was centered in the center cup and the alignment of all peaks was monitored. A gain calibration was performed at the start of every analytical session. Each analytical run was carried out in static acquisition mode and consisted of 24 blocks with 20 cycles each. The integration time of each cycle was 8.4 s. The amplifiers were rotated, and the baseline (30 cycles at 1.05 s per cycle) was measured after each block. The signal intensities of ^{50}Cr, ^{51}V, ^{52}Cr, ^{53}Cr, ^{54}Cr, ^{55}Mn, and ^{56}Fe were measured on the Faraday cups L3, L2, L1, C, H1, H2, and H3, respectively. Signal intensities of Cr, V, and Fe isotopes were measured using 10^{11} Ω resistors and a 10^{12} Ω resistor was used for for ^{55}Mn. Iron-56 and ^{51}V were measured to correct for isobaric interferences of ^{54}Fe on ^{54}Cr and ^{50}V on ^{50}Cr. The signal intensity of ^{51}V was always indistinguishable from the background intensity. The signal intensities of ^{52}Cr during the measurements were always between 7 and 10 V. Corrections for instrumental mass fractionation on $^{53}Cr/^{52}Cr$ and $^{54}Cr/^{52}Cr$ were made by normalizing to $^{52}Cr/^{50}Cr$ (=19.28323; Shields et al., 1966) and by applying the law for exponential mass fractionation. The terrestrial Cr standard reference material NIST SRM 979 was measured along with the samples, with a sample/standard ratio of 13:5. The results are reported in $\varepsilon^{i}Cr$ and are calculated via:

$$\varepsilon^{i}Cr = \left[\frac{(^{i}Cr/^{52}Cr)_{sample}}{(^{i}Cr/^{52}Cr)_{NIST\ SRM\ 979}} - 1\right] \times 10,000\ with\ i = 53, 54 \quad (1)$$

where $(\ ^{i}Cr/\ ^{52}Cr)_{NISTSRM979}$ is the mean of individual standard measurements (n = 5). The external precision (2SD) for NIST SRM 979 during this study was 0.090 for $\varepsilon^{53}Cr$ and 0.194 for $\varepsilon^{54}Cr$. For error calculation, 2SE values of 0.040 for $\varepsilon^{53}Cr$ and 0.087 for $\varepsilon^{54}Cr$ were used.

4. Results

4.1. Sample results

4.1.1. Petrography of the symplectites and veins

The Type II symplectites in the ungrouped ultramafic achondrites NWA 12217, 12319, 12562 (Vaci et al., 2021), the ungrouped achondrite QUE 93148 (Goodrich and Righter, 2000), the newly found meteorite NWA 13954 (Met. Bull.), and the harzburgitic clasts in howardites (Hahn et al., 2018) are composed of vermicular laths of chromite intergrown with low-Ca pyroxene, with minor high-Ca pyroxene, Fe-sulfide, and FeNi metal (Fig. 1). The widths of individual chromite laths range from 100 nm to 15 µm (Fig. 2). The compositions of the symplectic phases are largely uniform, with differences in the bulk compositions of the symplectites accounted for by differences in modal mineralogy.

NWA 12217 also contains veins composed of chromite and pyroxene that overlap in composition with the symplectites. The lengths of these veins range from hundreds of µm to tens of mm. The veins commonly host Type II symplectites as well, which splay out into bordering olivine grains (Fig. 3). The veins cut across individual olivine grains at random orientations, as the principal axes of the olivine grains cut by veins do not show any spatial trends in relation to the veins themselves (Fig. 4). This contrasts with Type I symplectites, which are observed having formed parallel or perpendicular to the (1 0 0) plane in olivine (Moseley, 1984; Mikouchi et al., 2000; Khisina and Lorenz, 2015). The micro-XCT scan shows that in 3D, the symplectic veins form large planar features oriented randomly throughout the breccia (Fig. 5; Supplementary Videos). Like the symplectites, symplectic veins are also associated with Fe-sulfide and FeNi metal (shown in red in Supplementary Video 2), although sulfides and metals are not resolved from one another in the XCT scan. Voxel counting of the XCT scan shows that symplectites compose 0.89 ± 0.30 vol% of the sample, which overlaps with an estimate using BSE greyscale thresholding (~1%).

The compositions of the phases within symplectites and symplectic veins are distinct from the compositional trends defined by the primary igneous phases of their host rock. The primary chromites and the symplectic chromites within symplectites and veins comprise two different trends in NWA 12217 and 12562 (Fig. 6). The higher Mg# and Cr# of the chromites in NWA 12217 is in accord with the higher Mg# of its olivine and its bulk rock composition (Vaci et al., 2021). Each trend in these rocks is distinct from the majority of HED chromite compositions (Mittlefehldt, 2015). In each rock, the symplectic chromites comprise

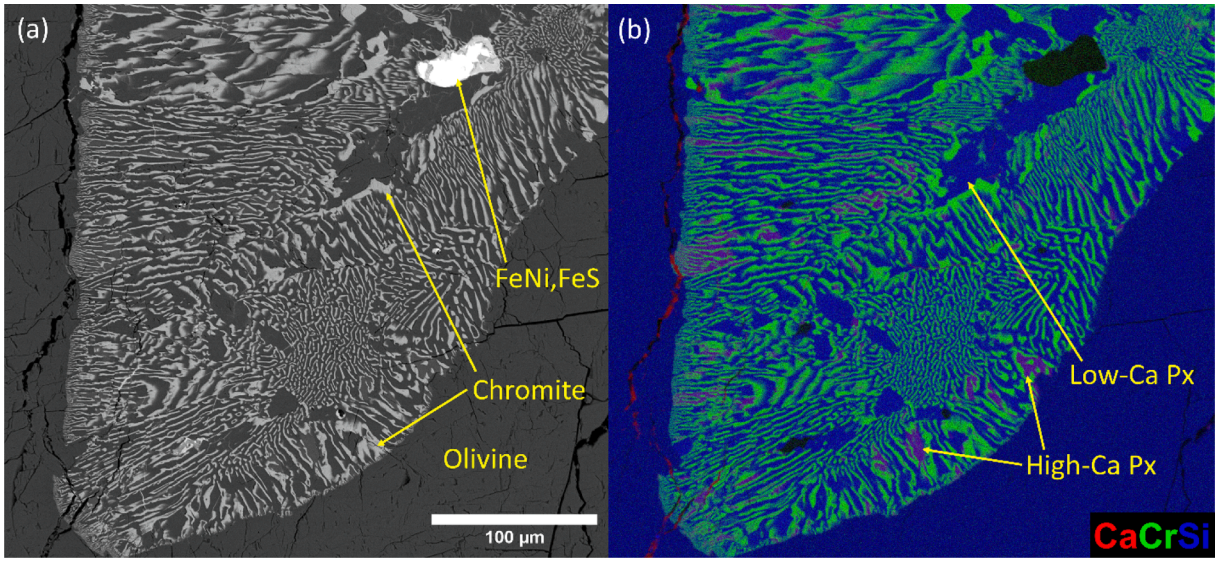

Fig. 1. BSE (a) and X-ray (b) images of a large Type II symplectite in NWA 12217. This symplectite is completely surrounded by olivine and lacks any vein-like features.

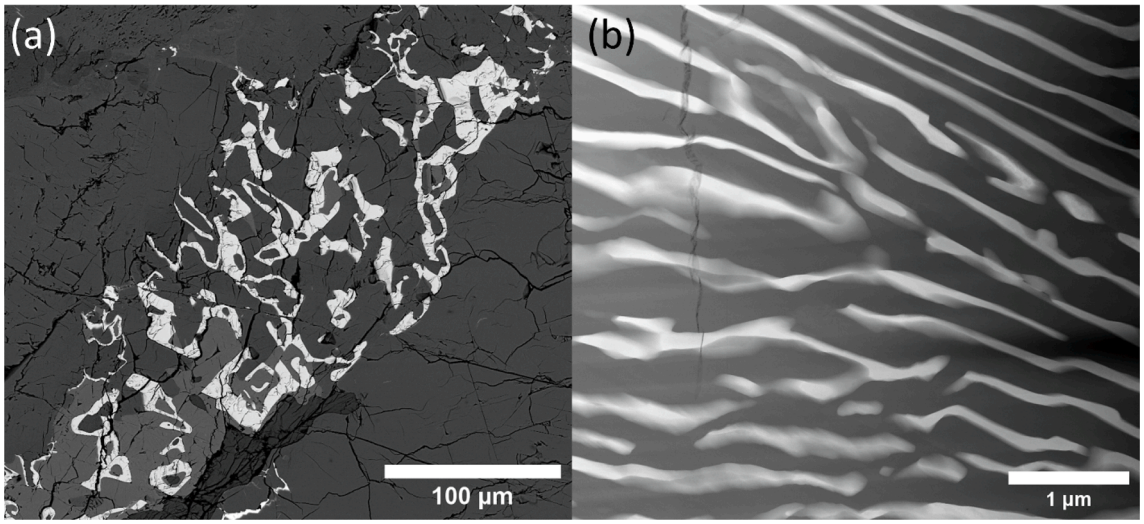

Fig. 2. BSE (a) and HAADF STEM (b) images of two different symplectites in NWA 12217. Lath thicknesses vary by three orders of magnitude.

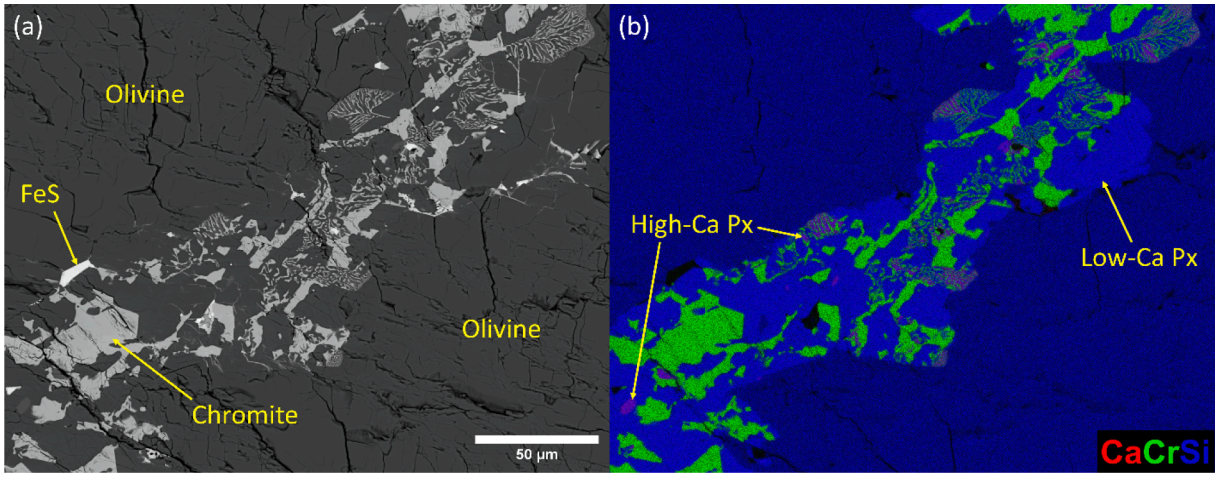

Fig. 3. BSE (a) and X-ray (b) images of a vein cutting across an olivine grain in NWA 12217. Symplectites are observed within the vein.

the Cr and Fe-rich end members. Although the symplectic and primary trends overlap, it is possible that they form two separate groups, since most of the data labelled as primary chromite in Fig. 6 is taken from Vaci et al. (2021), who did not distinguish between primary and symplectic chromite. Primary and symplectic chromites in NWA 12217 and 12562 clearly differ in composition. The compositions of pyroxenes in NWA 12217 and 12562 show an opposite trend to those of the chromites, with symplectic phases comprising Mg-rich endmembers and primary pyroxenes showing more Fe-rich compositions (Fig. 7).

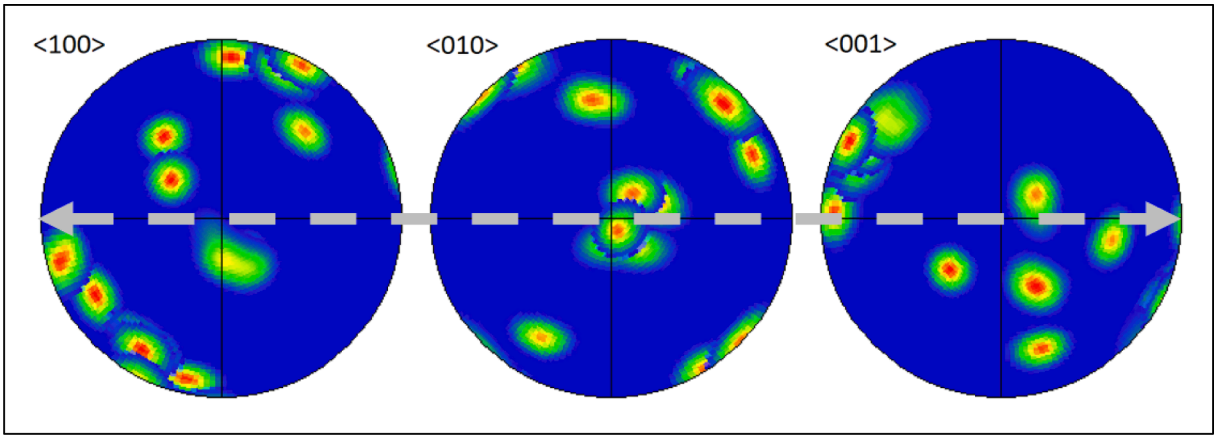

Fig. 4. Stacked pole figures for each of the principal axes of olivine grains cut by symplectic veins in NWA 12217, with grey dashed arrow representing the orientation of each vein. Color warmth corresponds to probability density of solutions for each axis.

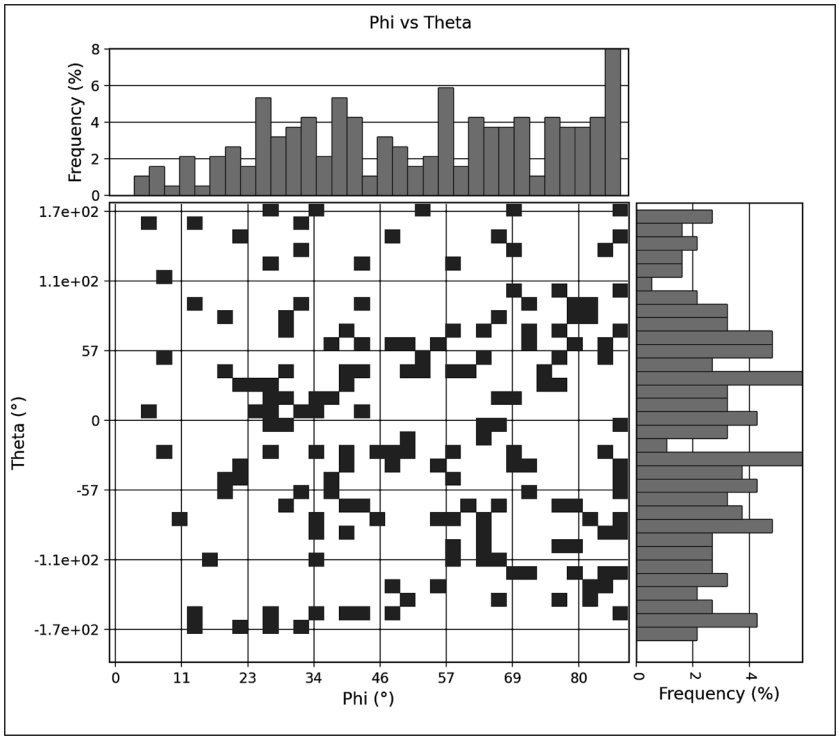

Fig. 5. Frequency distribution of Phi vs. Theta angles of the symplectic veins scattered throughout NWA 12217, showing a lack of any trends in orientation. Graph generated using Dragonfly software (Object Research Systems, 2022).

4.1.2. Chromium isotope systematics

The ε^{53}Cr, ε^{54}Cr, ^{55}Mn/^{52}Cr and Fe/Cr of all fractions from NWA 12217 are shown in Table 2. Fig. 12 shows the ^{54}Cr/^{52}Cr values of each individual measurement. The ε^{53}Cr and ε^{54}Cr values represent the mean of the individual measurements of each fraction with an uncertainty reported as 2 standard errors (2SE), which incorporate the uncertainty of the standard measurements. The terrestrial reference material OKUM and the meteorite Allende were measured previously (Anand et al., 2022) and are consistent with literature values, confirming the accuracy of the analytical method. The ε^{54}Cr value of the whole rock (ε^{54}Cr = -0.633 ± 0.141) agrees within the analytical uncertainty with the value determined by Vaci et al. (2021) (ε^{54}Cr = -0.68 ± 0.08). The ε^{53}Cr value of the whole-rock reported in Vaci et al. (2021) (ε^{53}Cr = -0.15 ± 0.03) is lower than the value in this study (ε^{53}Cr $_{WR}$=0.378 ± 0.071). The difference in ε^{53}Cr between the two studies suggests different proportions of mineral phases with different Mn/Cr in the samples. A mass balance calculation using ^{55}Mn/^{52}Cr of WR, L1, and L2 results in a mass fraction of 0.25 ± 0.07 wt% chromite in the homogenized WR powder.

The Fe/Cr of all fractions are ≲21 and their exposure to cosmic radiation was likely 6 to 73 Ma (Bekaert et al., 2022); therefore no correction for spallogenic Cr contributions is required (more details are provided in Supplementary Material). The ε^{54}Cr values of L1 and L2 are analytically distinct according to the following statistical tests. A two-sample student's *t*-test of the ^{54}Cr/^{52}Cr values for L1 and L2 rejects the hypothesis that L1 and L2 have the same mean value at the 95 % confidence interval, assuming unequal variances (p = 0.009) or equal variances (p = 0.011). Whereas the *t*-test looks for differences in the mean of the data assuming normality, the two sample Kolmogorov-Smirnov (K-S) test can be used to determine if L1 and L2 were drawn from the same underlying distribution without the assumption of normality. The null hypothesis that L1 and L2 are drawn from the same distribution is not rejected with the two-sample K-S test at the 95 % confidence interval (p = 0.053).

Another way to examine the difference between L1 and L2 is to construct confidence intervals. The sample standard deviation of the NIST SRM 979 standard ^{54}Cr/^{52}Cr is 2.742 × 10^{-7}, similar to L1 (2.740 × 10^{-7}) and L2 (2.100 × 10^{-7}). To account for the reproducibility of the standard measurements, the variance of the standard is added to the variances of the two samples to calculate the confidence interval of the ^{54}Cr/^{52}Cr ratio in L1 minus that of L2

$$\mathrm{CI}_{\alpha} = \left[\overline{\left(\frac{^{54}\mathrm{Cr}}{^{52}\mathrm{Cr}}\right)_{\mathrm{L1}}} - \overline{\left(\frac{^{54}\mathrm{Cr}}{^{52}\mathrm{Cr}}\right)_{\mathrm{L2}}}\right] \pm t(\alpha, n_{\mathrm{L1}}+n_{\mathrm{L2}}-2)\sqrt{\frac{s_{\mathrm{L1}}^2+s_{\mathrm{NIST}}^2}{n_{\mathrm{L1}}}+\frac{s_{\mathrm{L2}}^2+s_{\mathrm{NIST}}^2}{n_{\mathrm{L2}}}} \quad (2)$$

where n is the number of measurements (5 for L1 and 4 for L2), α is the confidence level, and t is the critical value of the t-distribution corresponding to the desired confidence level α and degrees of freedom n_{L1} + n_{L2} − 2. The means were calculated for both data sets, so two degrees of freedom must be subtracted from the n_{L1} + n_{L2} data points used to calculate the standard error of the difference. The interval for a 5% confidence level barely includes zero; a confidence level of 5.3% does not include zero.

Based on these statistical tests, ^{54}Cr/^{52}Cr in L1 is higher than that in L2 with a confidence higher than 1σ but less than 2σ. However, there are likely to be systematic errors unaccounted for in these statistics that may mean the measured separation between L1 and L2 is less than that of the pure end-member mineral phases, since there could have been partial equilibration between the symplectic veins and their silicate hosts. In summary, this suggests that NWA 12217 contains phases with Cr from at least one external source with a different isotopic composition. The mineral phases in the sample were never completely chemically homogenized.

The ε^{54}Cr of L1 (ε^{54}Cr = -0.527 ± 0.151) and L2 (ε^{54}Cr = -0.729 ± 0.150) are within the range of several non-carbonaceous achondrites (Supplementary Table S4). A correlation between ε^{53}Cr and ε^{54}Cr appears because L1 has an excess of ε^{53}Cr due to the in situ decay of ^{53}Mn and a higher ε^{54}Cr composition than L2, while L2 has a ^{55}Mn/^{52}Cr near zero. The excess in ^{53}Cr in the WR and L1 (ε^{53}Cr $_{WR}$=0.378 ± 0.037;

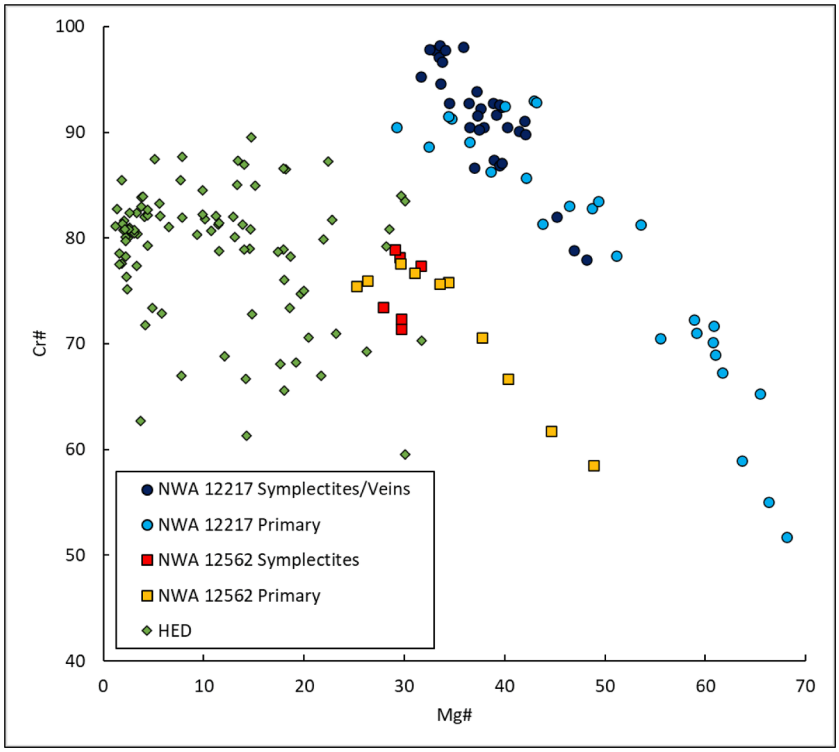

Fig. 6. Mg# [Mg/(Mg + Fe)] vs. Cr# [Cr/(Cr + Al)] for chromites found in NWA 12217, 12562, and HED meteorites. Some of the primary chromite data is from Vaci et al. (2021); HED data is from Mittlefehldt (2015).

$\varepsilon^{53}Cr_{L1} = 0.596 \pm 0.035$), relative to the terrestrial standard NIST SRM 979, suggests isotopic closure of the ^{53}Mn-^{53}Cr system in the first few million years of Solar System history. The ε^{53}Cr of L1 and L2 can be used to constrain model ages for the time of ^{55}Mn/^{52}Cr fractionation on their respective parent body by the intersection of their evolution curves with the chondritic evolution curve by

$$\Delta T_{X-CAI} = \frac{1}{\lambda_{53}} \ln\left[\frac{\left(^{53}Mn/^{55}Mn\right)_0}{\left(^{53}Mn/^{55}Mn\right)_{X-CI}}\right] \quad (3)$$

with

$$\left(^{53}Mn/^{55}Mn\right)_{X-CI} = \frac{\left(^{53}Cr/^{52}Cr\right)_X - \left(^{53}Cr/^{52}Cr\right)_{CI}}{\left(^{55}Mn/^{52}Cr\right)_X - \left(^{55}Mn/^{52}Cr\right)_{CI}} \quad (4)$$

and

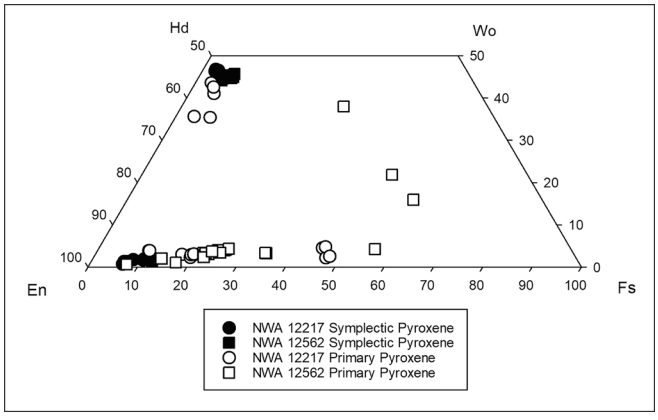

Fig. 7. Pyroxene quadrilateral diagram showing symplectic and primary pyroxene compositions in NWA 12217 and 12562. Some data from primary pyroxenes are from Vaci et al. (2021).

$$\left(^{53}Mn/^{55}Mn\right)_0 = \left(^{53}Mn/^{55}Mn\right)_{D'Orbigny} e^{\lambda_{53}\left(t_{CAI} - t_{D'Orbigny}\right)} \quad (5)$$

where $\left(^{55}Mn/^{52}Cr\right)_X$ and $\left(^{53}Cr/^{52}Cr\right)_X$ are the ratios of the sample (Table 2), the CI chondrite values are $\left(^{55}Mn/^{52}Cr\right)_{CI} = 0.84$ and $\varepsilon^{53}Cr_{CI} = 0.28$ (Zhu et al., 2021), the decay constant of ^{53}Mn (λ_{53}) is $\frac{\ln(2)}{t_{53}}$ with $t_{53} = 3.7$ Ma (Honda and Imamura, 1971), the $\left(^{53}Mn/^{55}Mn\right)_{D'Orbigny}$ of D'Orbigny angrite is 3.24×10^{-6} (Glavin et al., 2004), and the absolute ages of D'Orbigny angrite ($t_{D'Orbigny}$) and CAI (t_{CAI}) are 4563.51 Ma (Tissot et al., 2017) and 4567.3 Ma (Connelly et al., 2012), respectively. The resulting model ages for L1 and L2 are $3.11^{+0.65}_{-0.58}$ Ma and $2.87^{+2.01}_{-1.46}$ Ma after the formation of CAI, respectively (Fig. 13). Despite isotopic disequilibrium of ε^{54}Cr between L1 and L2, the ^{53}Mn-^{53}Cr systematics yield an isochron (Fig. 14), suggesting that the reservoirs of L1 and L2 formed simultaneously and evolved from a composition with initially similar CI-like ^{55}Mn/^{52}Cr. The isochron yields ^{53}Mn/^{55}Mn $= 3.81 \pm 0.60 \times 10^{-6}$, which corresponds to an age of $2.92^{+0.93}_{-0.79}$ Ma after the formation of CAI (CAI with an absolute Pb-Pb age of 4567.3 ± 0.16 Ma; Connelly et al., 2012), when anchored to the angrite D'Orbigny with ^{53}Mn/^{55}Mn $= 3.24 \pm 0.04 \times 10^{-6}$ (Glavin et al., 2004) and a U-corrected Pb-Pb age of 4563.51 ± 0.18 Ma (Tissot et al., 2017).

4.2. Experimental results

4.2.1. Symplectite melting experiments

The graphic texture of Type II symplectites suggests that they could have formed from residual melts that were multiply saturated in pyroxene and chromite (e.g. Bell et al., 1975). To test this hypothesis in regard to the ultramafic achondrites, melting experiments were conducted at 1 bar on bulk compositions that are similar to those determined using broad-beam electron microprobe measurements of symplectites. Two compositions were chosen with different amounts of high-Ca pyroxene (Table 1, Fig. 8). Experimental charges were heated to

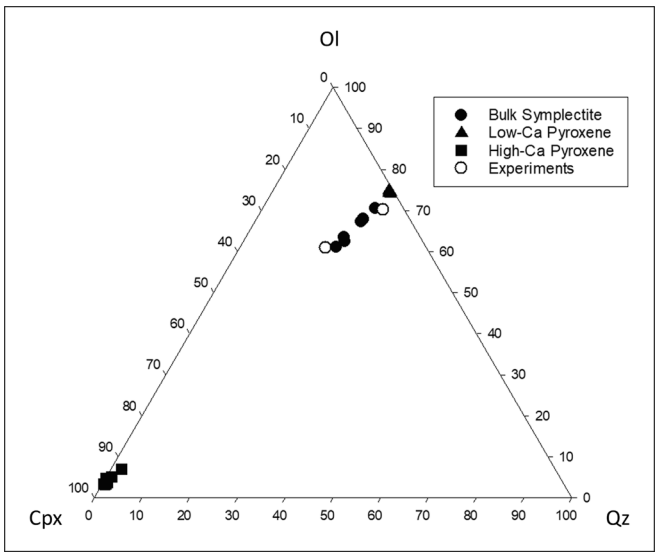

Fig. 8. Ternary diagram of bulk symplectite, symplectic pyroxene, and experimental compositions in olivine-quartz-clinopyroxene space, projected from chromite and plagioclase.

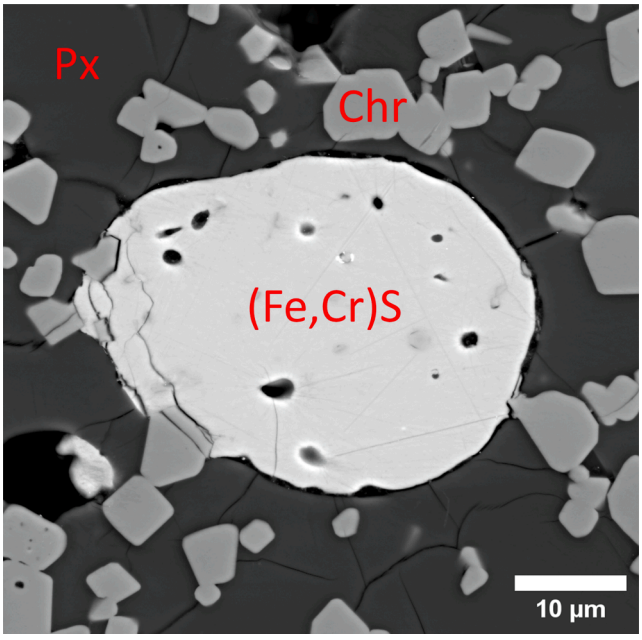

Fig. 9. BSE image of experimental Cr-bearing sulfide melt in experiment OD189. Px = pyroxene; Chr = chromite; (Fe,Cr)S=sulfide melt.

1400° C and resulted in fully crystalline run products in which no melting was observed, despite the large amount of melting expected for compositions near a minimum melting point. Therefore, additional components were explored to lower the melting temperatures of the experiments. Because small amounts of sulfide and metal are present within symplectites and veins, 4.3 wt% S was added in the form of synthetic FeS powder. The 4.3 wt% S was the maximum amount that could be added as FeS without altering the amount of Fe in the bulk composition. Sulfides were not present in the run products of initial melting experiments at one atmosphere, presumably due to vaporization during the runs, and therefore successive experiments using S-doped compositions were performed at 1 GPa in graphite capsules and Pt-jacketed graphite capsules in a piston-cylinder apparatus.

Electron microprobe analyses of the run products of the symplectite

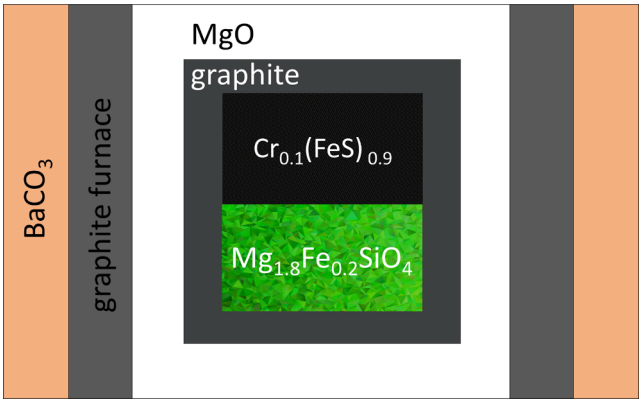

Fig. 10. Cross sectional schematic diagram (not to scale) of an experimental assemblage for symplectite experiments performed in a piston cylinder apparatus. The outer diameter of the graphite capsule is 4.5 mm.

melting experiments are shown in Supplementary Table S1. The results are similar across different experiments, with a groundmass consisting of chromites, pyroxenes, and minor silica. Sulfides were only present in experiments performed at 1 GPa. FeS grains were observed throughout the groundmass that contained 10–20 wt% Cr, but no melting was observed up to 1400° C. The highest temperature symplectite melting experiment was performed at 1500° C, and it produced Fe-S-Cr liquid of varying composition throughout the silicate groundmass. Blebs of this liquid with a diameter of ~ 10–30 µm were observed (Fig. 9), and these have Cr contents between 12 and 30 wt%, similar to what is calculated for the Fe-S-Cr ternary system (Waldner, 2014).

The measurement of Cr concentrations by electron microscopy in a system containing Fe is problematic due to the secondary fluorescence of Cr atoms by X-rays emitted by Fe atoms which can result in Cr abundances that are apparently higher than the actual value. While this fluorescence within the phase of interest is accounted for in the fluorescence correction, the correction does not account for neighboring phases. The attenuation of X-rays through the Fe-S-Cr liquid was calculated using the CalcZAF software package and the Beer-Lambert Law and was found to allow for significant fluorescence of up to ~ 50 µm from the incident electron beam. Microprobe points within the sulfide mass avoided such effects, however any measurement of Cr concentrations in sulfides adjacent to chromites is likely higher than the actual value by up to 40%.

4.2.2. *Olivine-sulfide reaction experiments*

The failure of the symplectite melting experiments to generate large amounts of melt or graphic textures prompted a second experimental scheme to generate symplectites. Chromium metal and FeS powder were mixed to obtain a bulk composition of $Cr_{0.1}(FeS)_{0.9}$. The powder was packed on top of gem-quality San Carlos olivine (Fo_{91}) grains that had been crushed and sieved to obtain a 150 µm size fraction. This bilayer assemblage (Fig. 10) was pressurized to 1 GPa and heated to 900° C overnight in order to compact the olivine crystals at a temperature below the sulfide eutectic and remove any void space from the charges. Experimental charges were then heated to between 1200 and 1400° C, i.e. above the liquidus of the Cr-Fe-S system (Waldner, 2014) and below the solidus of the MgO-FeO-SiO_2 system (Bowen and Schairer, 1935). They were then either quenched rapidly or allowed to cool to 1000° C at a rate of 60° C/min and then quenched.

SEM and microprobe analysis of the experimental run products showed extensive percolation of sulfide liquid throughout the olivine matrix. The reaction of the Cr-Fe-S liquid with olivine resulted in the formation of chromite and pyroxene, in accordance with the following idealized reaction:

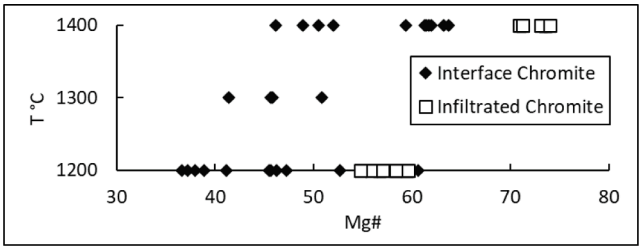

Fig. 11. Experimental chromites Mg# vs. the quench temperature of each experiment. Infiltrated chromites were not identified in the 1300 °C experiment, likely because of the slice location of the charge.

$$FeCr_2S_{4\,(liq)} + 4(Mg,Fe)_2SiO_4 \rightarrow (Mg,Fe)Cr_2O_4 + 2(Mg,Fe)_2Si_2O_6 + 3(Mg,Fe)S_{(liq)} + FeS_{(liq)} \quad (6)$$

A detailed image pyramid including BSE and X ray data of one of the percolation experiments can be found at https://presolar.physics.wustl.edu/qtool/OD193/. Supplementary Table S2 shows the microprobe analyses of chromites and pyroxenes in the olivine-sulfide reaction experiments. Pyroxene compositions are uniform and in Fe-Mg equilibrium with olivine reactants in each experiment, while variability in chromite composition is observed in all experimental run products regardless of variables such as temperature or cooling rate. This suggests that no experiments reached Fe-Mg equilibrium in chromite products. Chromites that formed interstitially to olivine grains as a result of sulfide infiltration are more magnesian than those that formed along the interface between the sulfide mass and the olivines, likely due to the availability of Mg (Fig. 11). While the minimum Mg# of analyzed chromites increases with experimental temperature, there is a large spread in Mg# at each experimental temperature. In the 1200° C experiment, the compositions of the interface chromites overlap with those of the infiltrated chromites. Overall, experimental chromite compositions reflect the disequilibrium of the reaction and preclude the use of Mg# as a thermometer.

Several control experiments were run to examine secondary processes that could affect the results of the olivine-sulfide experiments. One setup was held overnight at 900° C and then quenched. This

Table 1
Average of microprobe analyses on symplectites in NWA 12217 and synthetic experimental symplectite compositions.

wt.%	Symplectite avg. (n = 6)	Experimental Compositions			
		LowCa	HighCa	LowCa + S	HighCa + S
MgO	24.09	24.35	23.60	23.30	22.58
Al_2O_3	0.57	0.57	0.55	0.55	0.53
SiO_2	38.24	38.63	37.50	36.97	35.89
MnO	0.40	0.40	0.40	0.38	0.38
FeO	10.40	10.50	10.20	10.05	9.76
Cr_2O_3	24.18	24.50	23.70	23.45	22.68
TiO_2	0.05	0.05	0.05	0.05	0.05
CaO	2.48	1.00	4.00	0.96	3.83
S				4.31	4.31
Total	100.40	100	100	100	100

Table 2
$\varepsilon^{53}Cr$, $\varepsilon^{54}Cr$, $^{55}Mn/^{52}Cr$ and Fe/Cr of NWA 12217 fractions. The uncertainties of $\varepsilon^{53}Cr$ and $\varepsilon^{54}Cr$ are reported as 2 standard errors (2SE) based on the number of replicate measurements (N). The 2SE take into account the standard errors of the standard and sample measurements, along with the external reproducibility of the standard.

NWA 12,217	$\varepsilon^{53}Cr$	2SE	$\varepsilon^{54}Cr$	2SE	N	$^{55}Mn/^{52}Cr$	Fe/Cr
Whole rock	0.378	0.071	−0.633	0.141	4	1.35	15.24
L1 (silicates, sulfides, metals)	0.581	0.067	−0.527	0.151	5	1.77	21.05
L2 (symplectic chromites)	0.015	0.103	−0.729	0.150	4	0.063	<0.54

Table 3
Chromium isotope ratios with internal 2SE of individual measurements from this study. The ε-values are calculated for each analysis by Equation (1), where $^{i}Cr/^{52}Cr_{NIST\ SRM\ 979}$ is the average standard ratio. Each sample and standard is coded as Name(−fraction)_Filament_Run.

Sample or Standard	$^{53}Cr/^{52}Cr$	2SE uncertainty	$\varepsilon^{53}Cr$	$^{54}Cr/^{52}Cr$	2SE uncertainty	$\varepsilon^{54}Cr$
NISTSRM 979_1_1	0.11344177	0.00000068		0.02821066	0.00000033	
NISTSRM 979_1_2	0.11344151	0.00000071		0.02821105	0.00000039	
NISTSRM 979_2_1	0.11344115	0.00000068		0.02821104	0.00000036	
NISTSRM 979_3_1	0.11344049	0.00000056		0.02821080	0.00000029	
NISTSRM 979_4_1	0.11344161	0.00000066		0.02821040	0.00000034	
NISTSRM 979 average	0.11344131	0.00455661		0.02821079	0.00245283	
NWA 12217-WR_1_1	0.11344617	0.00000062	0.429	0.02820892	0.00000034	−0.663
NWA 12217-WR_1_2	0.11344563	0.00000063	0.381	0.02820915	0.00000031	−0.581
NWA 12217-WR_2_1	0.11344525	0.00000063	0.348	0.02820883	0.00000030	−0.694
NWA 12217-WR_2_2	0.11344531	0.00000056	0.353	0.02820911	0.00000029	−0.595
NWA 12217-L1_1_1	0.11344821	0.00000066	0.609	0.02820940	0.00000034	−0.494
NWA 12217-L1_2_1	0.11344828	0.00000072	0.615	0.02820894	0.00000035	−0.654
NWA 12217-L1_2_2	0.11344763	0.00000062	0.557	0.02820930	0.00000032	−0.527
NWA 12217-L1_3_1	0.11344813	0.00000061	0.601	0.02820919	0.00000032	−0.569
NWA 12217-L1_3_2	0.11344726	0.00000076	0.525	0.02820969	0.00000042	−0.390
NWA 12217-L2_1_1	0.11344053	0.00000067	−0.069	0.02820859	0.00000037	−0.779
NWA 12217-L2_1_2	0.11344082	0.00000070	−0.043	0.02820897	0.00000038	−0.647
NWA 12217-L2_2_1	0.11344220	0.00000062	0.079	0.02820885	0.00000032	−0.687
NWA 12217-L2_2_2	0.11344237	0.00000075	0.094	0.02820852	0.00000039	−0.804

Table 4
Summary of experiments. For notes, see Supplemental Table 3.

Exp.	Date	Setup	Starting Composition	fO_2	Pressure	Thermal Profile
J172	21/10/2021	Pressed pellet; Re loop	LowCa Symp.	IW-1	1 atm.	1300 °C for 24 h
J172-2	25/10/2021	Pressed pellet; Re loop	HighCa Symp.	IW-1	1 atm.	1400 °C for 20 h
H193	25/10/2021	Pressed pellet; Re loop	LowCa Symp.	IW-1	1 atm.	1400 °C for 20 h
J173	3/11/2021	Pressed pellet; Re loop	HighCa Symp. + 4.3 wt% S	IW-1	1 atm.	1300 °C for 20 h
J173-2	4/11/2021	Pressed pellet; Re loop	HighCa Symp. + 4.3 wt% S	IW-1	1 atm.	1400 °C for 20 h
H194	3/11/2021	Pressed pellet; Re loop	LowCa Symp. + 4.3 wt% S	IW-1	1 atm.	1300 °C for 20 h
H194-2	4/11/2021	Pressed pellet; Re loop	LowCa Symp. + 4.3 wt% S	IW-1	1 atm.	1400 °C for 20 h
OD182	16/11/2021	Graphite capsule; MgO ring	LowCa Symp. + 4.3 wt% S	CCO	1 GPa	1300 °C for 24 h
OD183	22/11/2021	Graphite capsule; MgO ring	HighCa Symp. + 4.3 wt% S	CCO	1 GPa	1300 °C for 24 h
OD184	2/12/2021	Graphite capsule; MgO ring	LowCa Symp. + 4.3 wt% S	CCO	1 GPa	1400 °C for 24 h
OD185	8/12/2021	Graphite capsule; MgO ring	HighCa Symp. + 4.3 wt% S	CCO	1 GPa	1400 °C for 24 h
OD186	15/12/2021	Graphite capsule; MgO ring	LowCa Symp. + 4.3 wt% S	CCO	1 GPa	600 °C for 4 h; 800 °C for 2 h; 1300 °C for 22 h; quench
OD187	31/1/2022	Graphite capsule; Pt Jacket; MgO ring	LowCa Symp. + 4.3 wt% S	CCO	1 GPa	1200 °C for 24 h
OD188	7/2/2022	Graphite capsule; Pt Jacket; MgO ring	HighCa Symp. + 4.3 wt% S	CCO	1 GPa	1200 °C for 24 h
OD189	25/2/2022	Graphite capsule; Pt Jacket; MgO ring	LowCa Symp. + 4.3 wt% S	CCO	1 GPa	1500 °C for 27 h
OD190	7/7/2022	Graphite capsule; MgO ring	Cr0.1(FeS)0.9 + S.C. Ol. Bilayer	CCO	1 GPa	900 °C overnight; 1400 °C 1.5 h; 60 °C/min. cooled to 1000 °C; quench
OD192	21/7/2022	Graphite capsule; MgO ring	Cr0.1(FeS)0.9 + S.C. Ol. Bilayer	CCO	1 GPa	900 °C overnight; quench
OD193	28/7/2022	Graphite capsule; MgO ring	Cr0.1(FeS)0.9 + S.C. Ol. Bilayer	CCO	1 GPa	900 °C overnight; 1400 °C 1 h; quench
OD194	3/8/2022	Graphite capsule; MgO ring	5 wt% $Cr_{0.1}(FeS)_{0.9}$ + 95 wt% S.C. Ol. Mix	CCO	1 GPa	900 °C for half day; quench (power failure)
OD195	22/8/2022	Graphite capsule; MgO ring	10 wt% $Cr_{0.1}(FeS)_{0.9}$ + 90 wt% S.C. Ol. Mix	CCO	1 GPa	900 °C overnight; 1400 °C 1 h; 60 °C/min. cooled to 1000 °C; quench
OD196	23/8/2022	Graphite capsule; MgO ring	FeS+S.C. Ol. Bilayer	CCO	1 GPa	900 °C overnight; 1400 °C 1 h; 60 °C/min. cooled to 1000 °C; quench
OD197	1/9/2022	Graphite capsule; MgO ring	$Cr_{0.1}(FeS)_{0.9}$	CCO	1 GPa	1400 °C 1.5 h; quench
OD198	21/9/2022	Graphite capsule; MgO ring	Cr0.1(FeS)0.9 + S.C. Ol. Bilayer	CCO	1 GPa	900 °C overnight; 1300 °C 1 h; quench
OD199	22/9/2022	Graphite capsule; MgO ring	Cr0.1(FeS)0.9 + S.C. Ol. Bilayer	CCO	1 GPa	900 °C overnight; 1200 °C 1 h; quench
OD200	28/11/2022	Graphite capsule; MgO ring	Cr0.1(FeS)0.9 + S.C. Ol. Bilayer	CCO	1 GPa	900 °C overnight; 1300 °C 1 h; quench
OD202	19/1/2023	Graphite capsule; MgO ring	FeS+S.C. Ol. Bilayer	CCO	1 GPa	900 °C overnight; 1400 °C 6 h; quench
OD203	23/1/2023	Graphite capsule; MgO ring	Cr0.1(FeS)0.9 + S.C. Ol. Bilayer	CCO	1 GPa	900 °C overnight; 1400 °C 6 h; quench
OD204	3/2/2023	Graphite capsule; MgO ring	Cr0.1(FeS)0.9 + S.C. Ol. Bilayer	CCO	1 GPa	900 °C overnight; 1200 °C 24 h; quench

experiment showed very little sulfide percolation into the olivine matrix and lacked any chromite or pyroxene formation, confirming that the annealing step closed pore space and avoided any sulfide melting. Another experiment consisted of a homogeneous mix of San Carlos olivine grains and 10 wt% $Cr_{0.1}(FeS)_{0.9}$ instead of a bilayer geometry. This showed a symplectic reaction network very similar to that of the bilayer. A control bilayer, using a Cr-free FeS powder, was also reacted with olivine at 1400° C for 1.5 h and cooled to 1000° C before quenching. This experiment showed extensive percolation of sulfide liquid through the olivine matrix, similarly to the experimental bilayers. Wüstite was identified along the edges of the sulfide mass, and minor magnesiowüstite was found interstitially within the percolated sulfide. Minor Fe enrichment along edges of olivine grains was also observed, suggesting that the Mg in the magnesiowüstite originated from olivine. Importantly, no pyroxene was observed, suggesting that the presence of Cr is integral to the symplectite-forming reaction. Finally, an experiment with $Cr_{0.1}(FeS)_{0.9}$ and no olivine was run at 1400° C to investigate oxide formation. Minor amounts of chromite grains were found along the bottom of the sulfide mass, suggesting that these formed as a result of oxygen contamination, which is unavoidable. Like the wüstite and magnesiowüstite in the control bilayer, they are unlikely to influence the symplectite-forming reaction. A summary of all experiments performed in this study are provided in Table 4 and Supplementary Table S3.

5. Discussion

5.1. Petrographic and geochemical evidence for sulfide melt percolation

The Type II symplectites in the ultramafic achondrites NWA 12217, 12319, 12562, and 13954 are texturally and compositionally indistinguishable from those found in harzburgite clasts in howardites (Hahn et al., 2018). Given the additional similarities in mineralogy and geochemistry between the ultramafic achondrites and these clasts, and the strong evidence that they also originate from Vesta or Vestoids (Vaci et al., 2021), it is likely that both sets of rocks are petrogenetically linked, and therefore their respective symplectites were formed by the same process. NWA 12217 is unique among these rocks in that its veins preserve evidence of the symplectite-forming process. The veins identified throughout NWA 12217 are mineralogically and geochemically identical to the symplectites they commonly contain (Figs. 3, 15). The morphologies (Fig. 5 and Supplementary Videos) and geometries of symplectic features relative to their host olivine grains (Fig. 4) also rule out any in situ formation process that has been suggested for Type I symplectites. The low Cr contents in all olivines vs. high amounts of chromite found in veins and symplectites in the ultramafic achondrites also argue for an exogenous Cr source. This is supported by the slight but significant difference in ε^{54}Cr of the chromites from the silicates.

The liquids that produced the veins and symplectites within NWA 12217 are likely to have formed by impact. The liquids that percolated through the rock had exotic compositions that are unlikely to have formed through magmatic differentiation. Instead, the chaotic impact of dunitic material with that of metallic and sulfidic lithology resulted in the creation of Cr-Fe-S and silicate liquids that percolated through the dunite and precipitated veins and symplectites. The most compelling evidence for an impact origin of the Cr-Fe-S liquid is the difference in ε^{54}Cr composition of the silicates and chromites in NWA 12217 (Table 2, Fig. 12). This difference is discussed in detail in the following section, but it results from a nucleosynthetic anomaly that is observed among meteorites that originate from parent bodies that formed in different regions of the solar nebula (e.g. Trinquier et al., 2007). The anomaly cannot be produced magmatically by any chemical fractionation process. Therefore, at least some of the Cr in the chromites must originate from a different ε^{54}Cr reservoir than the Cr in the olivine, and the Cr-Fe-S liquid was exogenous to the dunite.

The presence of high-Ca pyroxene within symplectites and veins in NWA 12217 suggests that a silicate melt was also present during the melt percolation process, as Ca would not fractionate into a sulfide or metallic melt at an oxygen fugacity that allows chromite precipitation.

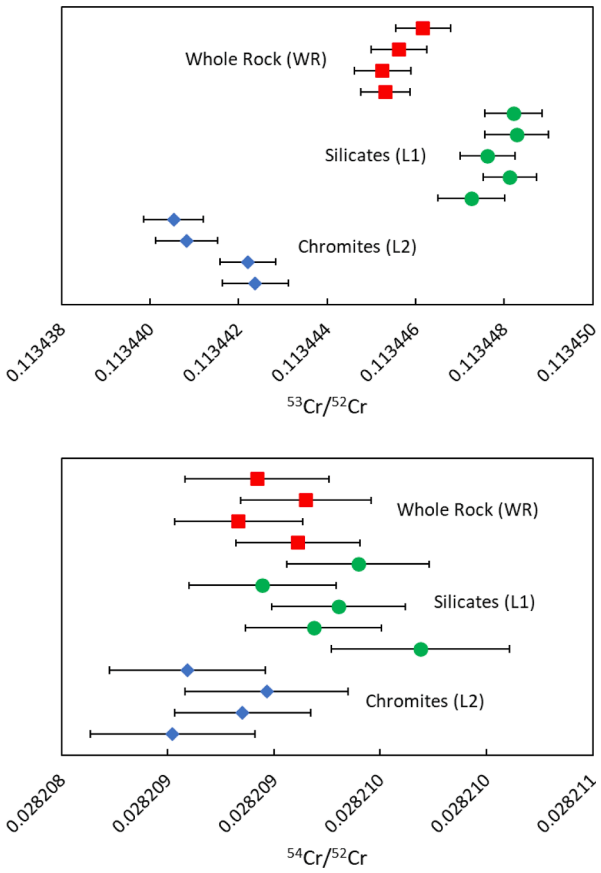

Fig. 12. $^{53}Cr/^{52}Cr$ and $^{54}Cr/^{52}Cr$ values of the whole rock (WR), silicate + metal (L1), and symplectic chromite residues (L2) in NWA 12217. Error bars are 2SE.

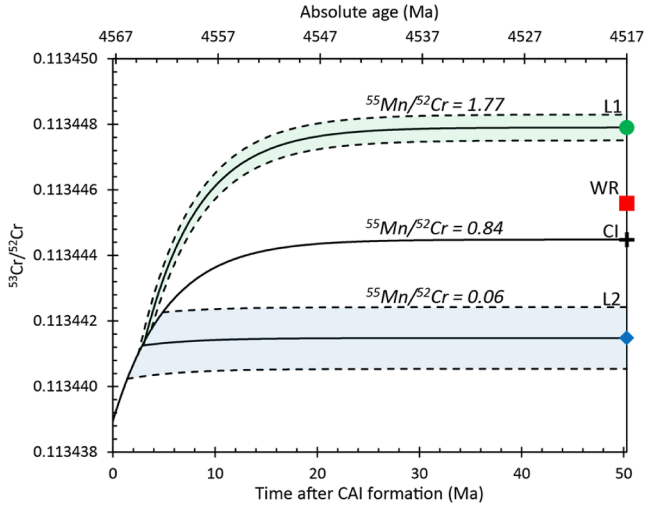

Fig. 13. Temporal evolution of the leach fractions from NWA 12217. The $\varepsilon^{53}Cr$ evolution curves of L1 and L2 are modeled by back-calculation from the measured $\varepsilon^{53}Cr$ composition. The corresponding ages for $^{55}Mn/^{52}Cr$ fractionation are given by Equation (3), assuming that both fractions are derived from a reservoir with CI-like composition.

The source of these silicate liquids is not necessarily exogenous, as the sulfide liquid could have partially melted and mobilized secondary phases such as feldspars which have been identified within the ultramafic achondrites (Vaci et al., 2021). More evidence is required to elaborate the nature of this silicate liquid, such as in situ measurements

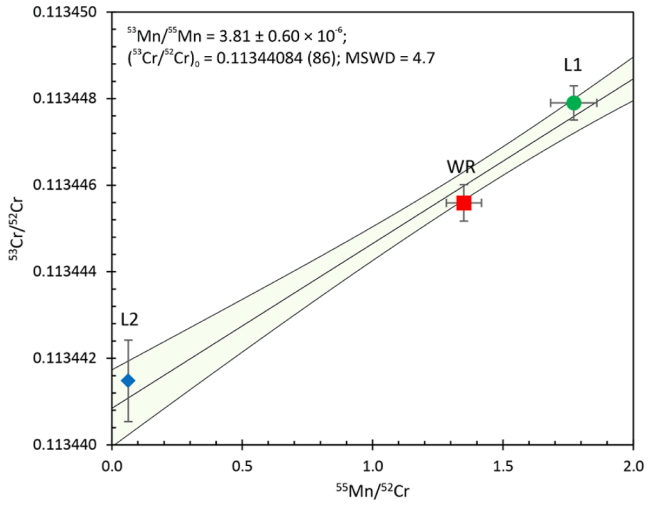

Fig. 14. Internal isochron of NWA 12217 constrained by WR, L1 and L2 fractions. CI chondrite from Zhu et al. (2021) is shown for comparison and suggests that NWA 12217 derived from a chondritic reservoir with CI chondrite-like $^{55}Mn/^{52}Cr$ and a canonical $\varepsilon^{53}Cr$ of the solar system constrained by CI chondrite.

of the trace element compositions of the various magmatic and symplectic phases in each of the ultramafic achondrites. However, as Ca is a minor component in the symplectites, its presence does not confound symplectite formation by sulfide percolation.

While the textures and orientations of the veins in NWA 12217 (Figs. 3, 4, 16) strongly suggests that a melt percolated through the dunite, the association between chromite and metal-sulfide assemblages is made clear by the XCT tomographic image (Supplementary Videos). There is an obvious association between metal-sulfide assemblages and chromite contained both in veins, isolated symplectites, and symplectites associated with veins. The presence of isolated symplectites is likely to result from later brecciation of the rock. By contrast, there are no isolated metal-sulfide blebs observed within the tomographic image.

5.2. *Isotope evidence for exogenous liquids*

The difference in ^{54}Cr between silicates (which are mostly olivine) and chromites identified in NWA 12217 is similar to the mass-independent O and ^{54}Cr isotope variations between olivines and chromites in pallasites recently identified by Windmill et al. (2022). In their model, two differentiated planetesimals collide, and the core of one is melted and injected into the mantle of the other, resulting in the mixed metal and olivine texture of the pallasites. This creates compositionally and isotopically heterogenous chromite grains, with low Cr# grains hypothesized to have crystallized from a silicate melt and high Cr# grains from a metallic melt. Similarly in NWA 12217 and 12562, symplectic chromite grains have higher Cr# than magmatic chromite grains since they crystallized from a sulfide liquid rather than a silicate melt. The $\varepsilon^{54}Cr$ heterogeneity between chromites (L2) and silicates (L1) in NWA 12217 suggests that the isotopic signature of chromite is dominated by symplectic rather than magmatic chromites. This dominance is also observed texturally in NWA 12217, which is riddled with symplectic veins (Supplementary Videos). By contrast, NWA 12319, 12562, and 13954 contain symplectites but no veins, likely because of impact brecciation that occurred after the symplectite forming process which only preserved fragments of their protolith (Vaci et al., 2021). Brecciation would obscure the origins of symplectic vein chromites and pyroxenes, as they lack the characteristic vermicular textures of Type II symplectites (Figs. 3, 15). Similarly, symplectites, but no symplectic veins, are identified in the harzburgite clasts present in howardites that are mineralogically and petrologically identical to NWA 12319, 12562,

and 13954 (Hahn et al., 2018). Additional in situ isotopic analyses are needed to determine whether the symplectite forming process is implicated in the heavier $\Delta^{17}O$ signature of NWA 12217 (Vaci et al., 2021) relative to the other ultramafic achondrites.

The $\varepsilon^{53}Cr$ model ages of L1 and L2 (Fig. 13) suggest that Mn/Cr fractionation occurred in the parent bodies of L1 and L2 nearly simultaneously. The good agreement of the two model ages suggests a similar evolution of the two parent bodies with similar initial $^{55}Mn/^{52}Cr$ and $\varepsilon^{53}Cr$ compositions. Since both bodies accreted in regions that were in close proximity within the non-carbonaceous chondrite (NC) reservoir, probably from the recently identified Vesta-like sub-reservoir (Rüfenacht et al., 2023), as indicated by their $\varepsilon^{54}Cr$ composition, an isochron can be constrained that informs on the time of Mn-Cr fractionation in the two parent bodies at $2.92^{+0.93}_{-0.79}$ Ma after the formation of CAI (Fig. 14). This age is in good agreement with the model ages of L1 and L2. These three ages overlap with the mantle differentiation ages of the HED parent body determined by ^{53}Mn-^{53}Cr chronometry (Lugmair and Shukolyukov, 1998; Trinquier et al., 2008) and postdate the metal-silicate fractionation age of ~ 1 Ma after CAI constrained by ^{182}Hf-^{182}W chronometry (Touboul et al., 2015). The early mantle differentiation and core formation ages of the parent bodies implies accretion within ~ 1–2 Ma of Solar System formation, followed by rapid heating and melting at a time when ^{26}Al was still abundant. This time coincides with the formation of iron meteorites (e.g. Anand et al., 2021b; Spitzer et al., 2021) and is slightly earlier than the accretion of undifferentiated ordinary and carbonaceous chondrites (e.g. Doyle et al., 2015; Anand et al., 2021a). It is likely that the impact that created the symplectites also occurred in this short interval of maximal planetesimal formation, when collisions of planetesimals were common (Morbidelli et al., 2009).

5.3. Experimental symplectic mineralogy

The experiments reproduced vein and symplectite mineralogy by reacting olivine with a Cr-Fe-S liquid which scavenges Fe and Mg from olivine to produce chromite and pyroxene (Fig. 16). This disequilibrium percolation reaction is a likely mechanism for the formation of Type II symplectites and veins in the ultramafic achondrites. Variable length scales of the vermicular symplectic textures could be produced by variable cooling rates, Cr availability, and addition of a silicate liquid that is likely the source of the Ca necessary to form the small amount of high-Ca pyroxene. This silicate liquid was not investigated experimentally because of the minor role that Ca plays in the symplectite formation process.

Importantly, sulfide percolation experiments performed without the

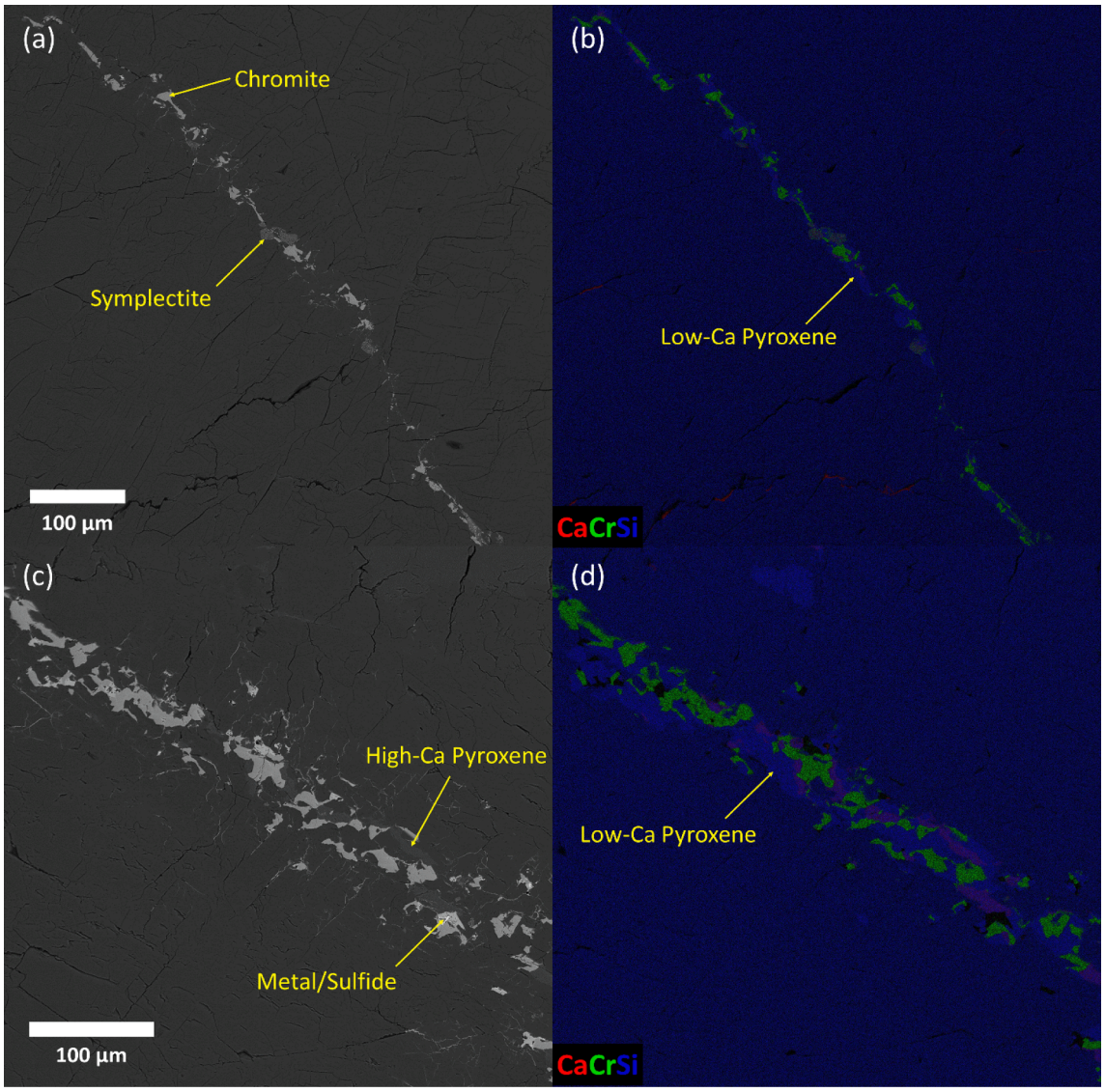

Fig. 15. BSE (a,c) and X-ray elemental (b,d) images of veins containing (a,b) and not containing (c,d) symplectites in NWA 12217.

addition of Cr failed to produce any oxide or silicate phases (Supplementary Table S3), suggesting that Cr is necessary to form symplectites. These are the first experiments that successfully reproduce the mineralogy of chromite-pyroxene symplectites in an ultramafic lithology. Future experiments could investigate other cations and their partitioning behavior relative to the FeS liquid and the olivine.

5.4. Solar System context of symplectite formation

Meteorite samples NWA 12217, 12319, 12562, 13954, and the harzburgite clasts within howardites (Hahn et al., 2018; Vaci et al., 2021) are all related to Vesta or the Vestoids, suggesting that the impact process that created the veins and symplectites involved either Vesta or the Vestoids. Type II symplectites are also identified within the ungrouped achondrite QUE 93148, which like the harzburgite clasts in howardites, were suspected to have formed via the interaction of a metallic and a silicate melt (Goodrich and Righter, 2000). These features could also have formed via sulfide melt percolation driven by an impact, and therefore this rock is also implicated with the HED meteorites and thus Vesta and Vestoids. Similar processes of impact-driven sulfide and metal induced metamorphism that results in symplectic textures have also been identified in the mesosiderite NWA 12949 (Wang and Tian, 2023). Finally, the Type II symplectites identified in the lunar troctolite 76535 were suggested to have formed via metasomatic infiltration of a Cr-saturated melt (Elardo et al., 2012), although the nature of that melt was mysterious. Although minor troilite was identified in association with reaction textures in lunar troctolite 76535, it was not considered as a potential Cr source for chromite formation. The experimental evidence

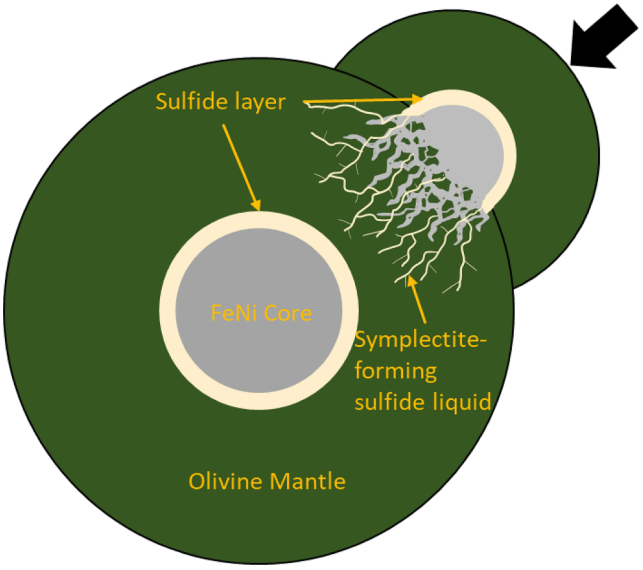

Fig. 17. Impact injection model for symplectite formation modified from the model of Windmill et al. (2022), in which the core of a small planetesimal is injected into the mantle of a larger one. The core contains a sulfide layer that is more easily mobilized than the metal and percolates throughout the olivine of the mantle, forming symplectites and symplectic veins.

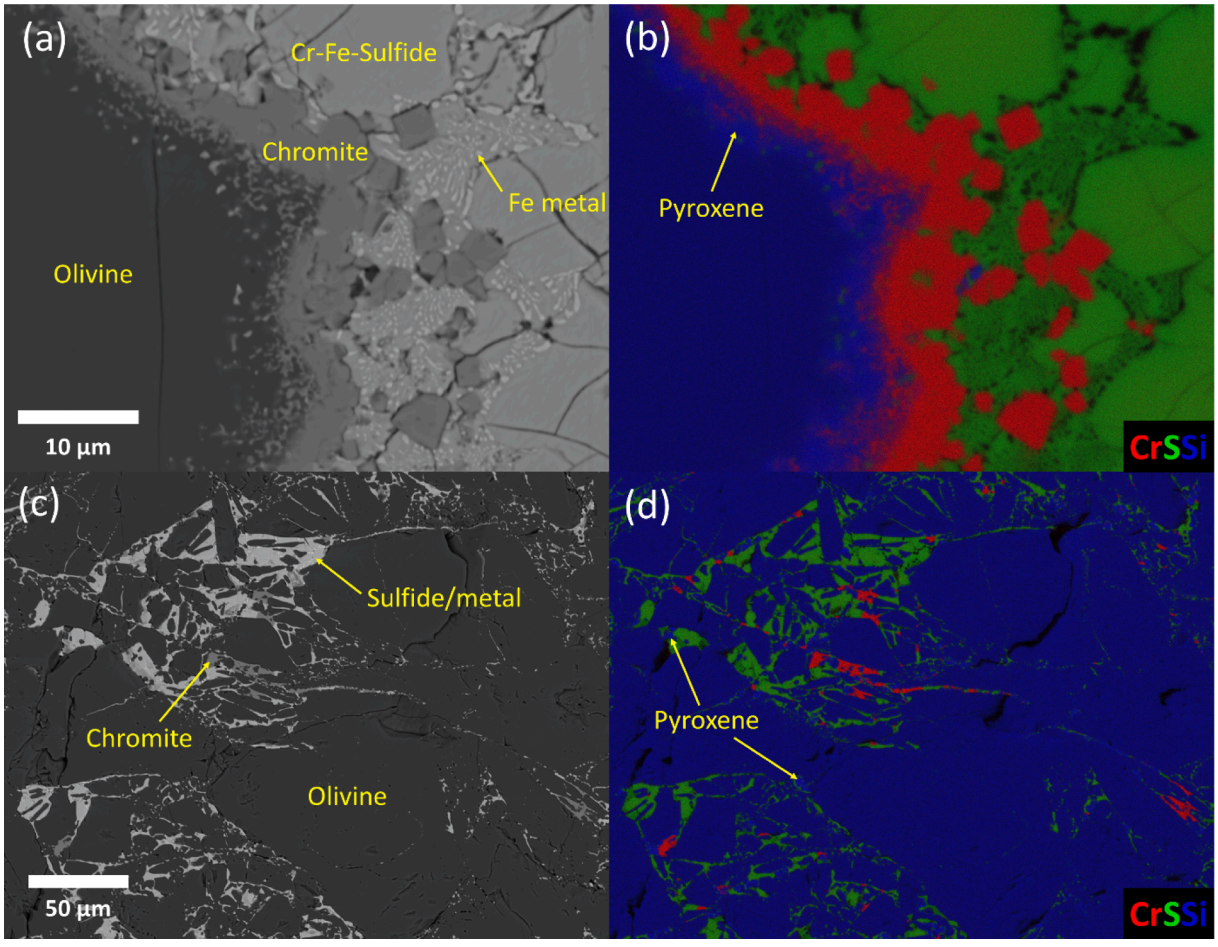

Fig. 16. BSE (a,c) and X-ray elemental (b,d) images of experimental run products showing the interface between the Cr-Fe-S liquid and olivine (a,b) and Cr-Fe-S liquid infiltration into olivine (c,d). Both show the same reaction that produces chromite and pyroxene.

presented in this study suggests that sulfide is a more plausible Cr source, given the extremely refractory nature of the symplectite bulk composition and the greater ability of a sulfide liquid to incorporate and mobilize Cr than a silicate melt. Whether the sulfide liquid in the lunar rock is impact-derived or the product of lunar magmatic processes needs further investigation.

One outstanding issue with the sulfide percolation symplectite formation model is the fate of the sulfide, as more Cr-Fe-S liquid is needed to produce symplectic textures than the preserved FeS grains suggest was present in the rocks. Therefore, the percolating melt network that formed symplectites and veins likely existed as an open system, and the Cr-Fe-S liquid was mostly lost. The ability of low viscosity sulfide melts to wet grain boundaries and form porous flow networks in olivine and chromite-rich rocks is well-documented (Gaetani and Grove, 1999; Brenan and Rose, 2002). Therefore, the symplectic textures observed in the ultramafic achondrites should be found at the fringes of the impact zone involving the core and mantle of a planetesimal (Windmill et al., 2022), where highly mobile sulfide melts are able to percolate further through an olivine-rich matrix than the metallic melts that are found in pallasites (Fig. 17). This type of impact requires a head-on collision to avoid mantle stripping (Asphaug et al., 2006; Cambioni et al., 2021) and relatively low speed (<5 km/s) so that the core of the impactor can be preserved in the mantle of the target (Maurel et al., 2020).

6. Conclusions

The spinel pyroxene symplectites in ultramafic planetary materials are products of the impact-driven infiltration of a Fe-Cr-S liquid. While garnet breakdown, fluid-assisted metasomatism, and oxidation are well characterized processes for forming planetary symplectites, small bodies lack the pressures required for garnet formation, the fluids necessary for metasomatism, or the redox conditions for oxidation. Thus, extraterrestrial samples containing spinel-pyroxene symplectites have had a host of formation scenarios attributed to them which usually implicated one or more exotic melts or fluids (Bell et al., 1975; Elardo et al., 2012; Hahn et al., 2018). This study is the first to experimentally generate such a melt capable of forming the relevant symplectic mineralogy present in natural samples. A Cr-Fe-S melt can generate chromite and pyroxene by percolating through olivine grains and forming a network of symplectic veins as is observed in NWA 12217. Spinel-pyroxene symplectites are products of specific cooling regimes within the melt percolation regime. We suggest that the texture, chemistry, and isotopic composition of the different components of this meteorite are the result of an impact process involving the partial mixing of differentiated planetary bodies that formed in separate isotopic reservoirs during the first ~ 3 Ma of Solar System history.

CRediT authorship contribution statement

Z. Váci: Writing – review & editing, Writing – original draft, Visualization, Validation, Supervision, Software, Resources, Project administration, Methodology, Investigation, Formal analysis, Data curation. **P. M. Kruttasch:** Writing – review & editing, Writing – original draft, Methodology, Investigation, Formal analysis, Data curation. **M.J. Krawczynski:** Writing – review & editing, Writing – original draft, Supervision, Project administration, Methodology, Investigation, Funding acquisition, Formal analysis, Conceptualization. **R.C. Ogliore:** Writing – review & editing, Writing – original draft, Software, Resources, Methodology, Investigation. **K. Mezger:** Writing – review & editing, Writing – original draft, Supervision, Methodology, Investigation.

Data availability

Data are available through WashU Research Data at https://doi.org/10.7936/6RXS-103631.

Declaration of competing interest

The authors declare that they have no known competing financial interests or personal relationships that could have appeared to influence the work reported in this paper.

Acknowledgements

The authors are grateful for the Institute of Meteoritics at the University of New Mexico for providing the meteorite samples analyzed in this study. We also thank the various instrument operators and laboratory personnel without whose technical expertise this would not have been possible, including Paul Carpenter and the WashU microprobe lab, Hélène Couvy Craigg and the Experimental Studies of Planetary Materials Lab, Clive Jones and the WashU SIMS lab, Huafang Li and the Institute of Materials Science and Engineering, and Peter Bayguinov and the Center for Cellular Imaging. XRM data was with support from the Office of Research Infrastructure Programs (ORIP), a part of the NIH Office of the Director under grant OD021694. Financial support for this study was provided by the Swiss National Science Foundation grant 188592.

Appendix A. Supplementary material

Supplementary material to this article can be found online at https://doi.org/10.1016/j.gca.2024.08.011.

References

Anand, A., Pape, J., Wille, M., Mezger, K., 2021a. Chronological constraints on the thermal evolution of ordinary chondrite parent bodies from the ^{53}Mn-^{53}Cr system. Geochim. Cosmochim. Acta 307, 281–301.

Anand, A., Pape, J., Wille, M., Mezger, K., Hofmann, B., 2021b. Early differentiation of magmatic iron meteorite parent bodies from Mn–Cr chronometry. Geochem. Persp. Let. 20, 6–10.

Anand, A., Kruttasch, P.M., Mezger, K., 2022. ^{53} Mn- ^{53} Cr chronology and ε^{54} Cr-Δ^{17} O genealogy of Erg Chech 002: The oldest andesite in the solar system. Meteorit. & Planet. Sci. 57, 2003–2016.

Asphaug, E., Agnor, C.B., Williams, Q., 2006. Hit-and-run planetary collisions. Nature 439, 155–160.

Bekaert, D.V., Curtice, J., Meier, M.M.M., Byrne, D.J., Broadley, M.W., Seltzer, A., Barry, P., Kurz, M.D., Nielsen, S.G., 2022. Determining the noble gas cosmic ray exposure ages of 23 meteorites (8 chondrites and 15 achondrites) from modeling and empirical methods. Meteorit & Planetary Scien 57, 1542–1569.

Bell, P.M., Mao, H.K., Roedder, E., Weiblen, P.W., 1975. The problem of the origin of symplectites in olivine-bearing lunar rocks. In: *Lunar and Planetary Science Conference Proceedings*, pp. 231–248.

Bowen, N.L., Schairer, J.F., 1935. The system MgO-FeO-SiO_2. Am. J. Sci. 5–29, 151.

Brenan, J.M., Rose, L.A., 2002. Experimental constraints on the wetting of chromite by sulfide liquid. Can. Mineral. 40, 1113–1126.

Cambioni, S., Jacobson, S.A., Emsenhuber, A., Asphaug, E., Rubie, D.C., Gabriel, T.S.J., Schwartz, S.R., Furfaro, R., 2021. The effect of inefficient accretion on planetary differentiation. Planet. Sci. J. 2, 93.

Connelly, J.N., Bizzarro, M., Krot, A.N., Nordlund, Å., Wielandt, D., Ivanova, M.A., 2012. The absolute chronology and thermal processing of solids in the solar protoplanetary disk. Science 338, 651–655.

Dawson, J.B., Smith, J.V., 1975. Chromite-silicate intergrowths in upper-mantle peridotites. Phys. Chem. Earth 9, 339–350.

Donovan, J., Kremser, D., Fournelle, J., Goemann, K., 2012. Probe for EPMA: acquisition, automation and analysis. Probe Software Inc, Eugene, Oregon.

Doyle, P.M., Jogo, K., Nagashima, K., Krot, A.N., Wakita, S., Ciesla, F.J., Hutcheon, I.D., 2015. Early aqueous activity on the ordinary and carbonaceous chondrite parent bodies recorded by fayalite. Nat Commun 6, 7444.

Dymek, R.F., Albee, A.L., Chodos, A.A., 1975. Comparative petrology of lunar cumulate rocks of possible primary origin: dunite 72415, troctolite 76535, norite 78235, and anorthosite 62237. Lunar and Planetary Science Conference Proceedings 1, 301–341.

Efimov, A.A., Malitch, K.N., 2012. Magnetite-orthopyroxene symplectites in gabbros of the Urals: A structural track of olivine oxidation. Geol. Ore Deposits 54, 531–539.

Elardo, S.M., McCubbin, F.M., Shearer, C.K., 2012. Chromite symplectites in Mg-suite troctolite 76535 as evidence for infiltration metasomatism of a lunar layered intrusion. Geochim. Cosmochim. Acta 87, 154–177.

Field, S.W., 2008. Diffusion, discontinuous precipitation, metamorphism, and metasomatism: The complex history of South African upper-mantle symplectites. Am. Mineral. 93, 618–631.

Gaetani, G.A., Grove, T.L., 1999. Wetting of mantle olivine by sulfide melt: implications for Re/Os ratios in mantle peridotite and late-stage core formation. Earth Planet. Sci. Lett. 169, 147–163.
Gavrilenko, M., Krawczynski, M., Ruprecht, P., Li, W., Catalano, J.G., 2019. The quench control of water estimates in convergent margin magmas. Am. Mineral. 104, 936–948.
Glavin, D.P., Kubny, A., Jagoutz, E., Lugmair, G.W., 2004. Mn-Cr isotope systematics of the D'Orbigny angrite. Meteorit. Planet. Sci. 39, 693–700.
Godard, G., Martin, S., 2000. Petrogenesis of kelyphites in garnet peridotites: a case study from the Ulten zone, Italian Alps. J. Geodyn. 30, 117–145.
Goodrich, C.A., Harlow, G.E., Van Orman, J.A., Sutton, S.R., Jercinovic, M.J., Mikouchi, T., 2014. Petrology of chromite in ureilites: Deconvolution of primary oxidation states and secondary reduction processes. Geochim. Cosmochim. Acta 135, 126–169.
Goodrich, C.A., Righter, K., 2000. Petrology of unique achondrite queen alexandra range 93148: A piece of the pallasite (howardite-eucrite-diogenite?) parent body? Meteorit. Planet. Sci. 35, 521–535.
Goodrich, C.A., Sutton, S.R., Wirick, S., Jercinovic, M.J., 2013. Chromium valences in ureilite olivine and implications for ureilite petrogenesis. Geochim. Cosmochim. Acta 122, 280–305.
Gooley, R., Brett, R., Warner, J., Smyth, J.R., 1974. A lunar rock of deep crustal origin: sample 76535. Geochim. Cosmochim. Acta 38, 1329–1339.
Greenwood, R.C., Barrat, J.-A., Scott, E.R.D., Haack, H., Buchanan, P.C., Franchi, I.A., Yamaguchi, A., Johnson, D., Bevan, A.W.R., Burbine, T.H., 2015. Geochemistry and oxygen isotope composition of main-group pallasites and olivine-rich clasts in mesosiderites: Implications for the "Great Dunite Shortage" and HED-mesosiderite connection. Geochim. Cosmochim. Acta 169, 115–136.
Hahn, T.M., Lunning, N.G., McSween, H.Y., Bodnar, R.J., Taylor, L.A., 2018. Mg-rich harzburgites from Vesta: Mantle residua or cumulates from planetary differentiation? Meteorit Planet Sci 53, 514–546.
Holness, M.B., Stripp, G., Humphreys, M.C.S., Veksler, I.V., Nielsen, T.F.D., Tegner, C., 2011. Silicate liquid immiscibility within the crystal mush: Late-stage magmatic microstructures in the Skaergaard intrusion, East Greenland. J. Petrol. 52, 175–222.
Honda, M., Imamura, M., 1971. Half-life of Mn 53. Phys. Rev. C 4, 1182–1188.
Iannini, L.S., Folco, L., Masotta, M., Greenwood, R.C., Russell, S.S., Bates, H.C., 2022. Asteroids accretion, differentiation, and break-up in the Vesta source region: Evidence from cosmochemistry of mesosiderites. Geochim. Cosmochim. Acta 329, 135–151.
Keevil, H.A., Namur, O., Holness, M.B., 2020. Microstructures and late-stage magmatic processes in layered mafic intrusions: Symplectites from the sept iles intrusion, quebec, canada. J. Petrol. 61, egaa071.
Khisina, N.R., Lorenz, C.A., 2015. Dehydrogenation as the mechanism of formation of the oriented spinel-pyroxene symplectites and magnetite-hematite inclusions in terrestrial and extraterrestrial olivines. Petrology 23, 176–188.
Khisina, N.R., Wirth, R., Nazarov, M.A., 2011. Lamellar pyroxene-spinel symplectites in lunar olivine from the Luna 24 regolith. Geochem. Int. 49, 449–458.
Lugmair, G.W., Shukolyukov, A., 1998. Early solar system timescales according to ^{53}Mn-^{53}Cr systematics. Geochim. Cosmochim. Acta 62, 2863–2886.
Lunning, N.G., McSween, H.Y., Tenner, T.J., Kita, N.T., Bodnar, R.J., 2015. Olivine and pyroxene from the mantle of asteroid 4 Vesta. Earth Planet. Sci. Lett. 418, 126–135.
Maurel, C., Bryson, J.F.J., Lyons, R.J., Ball, M.R., Chopdekar, R.V., Scholl, A., Ciesla, F.J., Bottke, W.F., Weiss, B.P., 2020. Meteorite evidence for partial differentiation and protracted accretion of planetesimals. Sci. Adv. 6, eaba1303.
Mikouchi, T., Yamada, I., Miyamoto, M., 2000. Symplectic exsolution in olivine from the Nakhla martian meteorite. Meteorit. Planet. Sci. 35, 937–942.
Mittlefehldt, D.W., 2015. Asteroid (4) Vesta: I. The howardite-eucrite-diogenite (HED) clan of meteorites. Geochemistry 75, 155–183.
Morbidelli, A., Bottke, W.F., Nesvorný, D., Levison, H.F., 2009. Asteroids were born big. Icarus 204, 558–573.
Morishita, T., Arai, S., 2003. Evolution of spinel–pyroxene symplectite in spinel–lherzolites from the Horoman Complex, Japan. Contrib Mineral Petrol 144, 509–522.
Moseley, D., 1984. Symplectic exsolution in olivine. Am. Mineral. 69, 139–153.
Object Research Systems (2022) Dragonfly 2022.1.
Putnis, A., Austrheim, H., 2010. Fluid-induced processes: metasomatism and metamorphism. Geofluids 10, 254–269.
Rüfenacht, M., Morino, P., Lai, Y.-J., Fehr, M.A., Haba, M.K., Schönbächler, M., 2023. Genetic relationships of solar system bodies based on their nucleosynthetic Ti isotope compositions and sub-structures of the solar protoplanetary disk. Geochim. Cosmochim. Acta 355, 110–125.
Shields, W.R., Murphy, T.J., Catanzaro, E.J., Garner, E.L., 1966. Absolute isotopic abundance ratios and the atomic weight of a reference sample of chromium. J. RES. NATL. BUR. STAN. SECT. a. 70A, 193.
Spitzer, F., Burkhardt, C., Nimmo, F., Kleine, T., 2021. Nucleosynthetic Pt isotope anomalies and the Hf-W chronology of core formation in inner and outer solar system planetesimals. Earth Planet. Sci. Lett. 576, 117211.
Spruzeniece, L., Piazolo, S., Daczko, N.R., Kilburn, M.R., Putnis, A., 2017. Symplectite formation in the presence of a reactive fluid: insights from hydrothermal experiments. J. Metamorph. Geol. 35, 281–299.
Tissot, F.L.H., Dauphas, N., Grove, T.L., 2017. Distinct ^{238}U/^{235}U ratios and REE patterns in plutonic and volcanic angrites: Geochronologic implications and evidence for U isotope fractionation during magmatic processes. Geochim. Cosmochim. Acta 213, 593–617.
Touboul, M., Sprung, P., Aciego, S.M., Bourdon, B., Kleine, T., 2015. Hf–W chronology of the eucrite parent body. Geochim. Cosmochim. Acta 156, 106–121.
Trinquier, A., Birck, J., Allegre, C.J., 2007. Widespread ^{54}Cr heterogeneity in the inner solar system. ApJ 655, 1179–1185.
Trinquier, A., Birck, J.-L., Allègre, C.J., Göpel, C., Ulfbeck, D., 2008. ^{53}Mn–^{53}Cr systematics of the early solar system revisited. Geochim. Cosmochim. Acta 72, 5146–5163.
Vaci, Z., Day, J.M.D., Paquet, M., Ziegler, K., Yin, Q.-Z., Dey, S., Miller, A., Agee, C., Bartoschewitz, R., Pack, A., 2021. Olivine-rich achondrites from Vesta and the missing mantle problem. Nat Commun 12, 5443.
Waldner, P., 2014. Thermodynamic modeling of the Cr-Fe-S System. Metall and Mat Trans A 45, 798–814.
Wang, Z., Tian, W., 2023. Petrology and mineralogy of mesosiderite Northwest Africa 12949: Implications for geological history on its parent body. Meteorit & Planetary Scien 58, 341–359.
Windmill, R.J., Franchi, I.A., Hellmann, J.L., Schneider, J.M., Spitzer, F., Kleine, T., Greenwood, R.C., Anand, M., 2022. Isotopic evidence for pallasite formation by impact mixing of olivine and metal during the first 10 million years of the Solar System. PNAS Nexus, p. gac015.
Zhu, K., Moynier, F., Schiller, M., Alexander, C.M.O., Davidson, J., Schrader, D.L., van Kooten, E., Bizzarro, M., 2021. Chromium isotopic insights into the origin of chondrite parent bodies and the early terrestrial volatile depletion. Geochim. Cosmochim. Acta 301, 158–186.